Small microbialites from the basal Triassic mudstone (Tieshikou, Jiangxi, South China): geobiologic features, biogenicity, and paleoenvironmental implications

Hao Yang[a], Zhong-Qiang Chen[a, *], Stephen Kershaw[b], Wei Liao[a], Enlü Lü[a], Yuangen Huang[a]

[a] State Key Laboratory of Biogeology and Environmental Geology, China University of Geosciences (Wuhan), Wuhan 430074, China

[b] Department of Life Sciences, Brunel University, Kingston Lane, Uxbridge, UB8 3PH, UK

*Corresponding author (Z.Q. Chen): E-mail address: zhong.qiang.chen@cug.edu.cn

Abstract

We report small microbialites from the calcareous mudstone slightly above the Permian−Triassic boundary (PTB) in the Tieshikou section, southern Jiangxi Province, South China. The newly found microbialite is a bowl-like structure, which contrasts with the surrounding calcareous mudstone. The small microbialite is composed of columnar forms and fan-shaped structures. Mini-columnar structures resemble mini stromatolites. In plane view, most branches are patchy or strip-shaped, with clotted structures, resembling that of a thrombolite. Fan-shaped cement precipitates are comprised of multiple crystal fans that have a radiating texture that show distinct growth laminae. The radiating fabrics are represented by rod-shaped filaments under SEM, which are interpreted as calcified trichomes/filaments. Prominent micropores occur within the rods, and they may be the plane views of multiple sheaths of the false branching zone of trichomes. Thus, both the columnar forms and radiating fans are

probably microbial in origin. Moreover, three types of nano-sized structures: intraparticle micropores, fibrous biofilms, and filamentous sheaths are also pronounced in both the columnar structures and cement fans of the Tieshikou microbialite, all suggestive of biogenicity. These well-preserved fibrous biofilms probably represent calcified extracellular polymeric substances (EPS), and linear sheaths are interpreted as the traces of bacterial activities during the precipitation of dolomite crystals. The Tieshikou microbialite therefore shares similar biogenetic mechanisms with other PTB microbialites. The combination of the absence of pyrite framboids, slightly negative carbon isotope values, and an association with abundant ammonoids, bivalves, and gastropods indicates oxic conditions during the growth of the Tieshikou microbialite. Moreover, the nodular preservational state resembles widely distributed nodular mudstones or muddy limestones of the Lower Triassic successions worldwide. This implies that nodular mudstone or argillaceous limestones might also be deposited in microbe-rich environments, in which terrigenous supply was also abundant.

Key words: mass extinction; Early Triassic; limestone nodule; carbonate precipitate; clotted structure; filamentous structures; microbial bloom

1. Introduction

Widespread microbialites (stromatolites, thrombolites, and dendrolites) characterize carbonate facies of Permian−Triassic boundary (PTB) beds in the Paleo-Tethys region (Kershaw et al., 2012), and often form pronounced microbial build-ups. These PTB microbialites usually overly the end-Permian mass extinction

51 horizon, and thus are related to the biotic extinction and subsequent harsh
52 environments (Kershaw et al., 2012; Lehrmann et al., 2015). Although some studies
53 clarify that the irregular clotted micritic structures and coccoid-like objects are
54 suggestive of the microorganisms that constructed the PTB calcimicrobial buildups
55 (Kershaw et al., 1999, 2002, 2007, 2012; Lehrmnn, 1999; Ezaki et al., 2003, 2008;
56 Wang et al., 2005; Yang et al., 2011; Wu et al., 2014, 2016, 2017; Lehrmann et al.,
57 2015; Tang et al., 2017; Fang et al., 2017; Bagherpour et al., 2017; Friesenbichler et
58 al., 2018; Pei et al., 2018), their accretion process and mechanism have long remained
59 enigmatic. Chen and Benton (2012) also hypothesized that the resurgence of
60 microbial buildups immediately after the end-Permian ecologic crisis signals a
61 calcimicrobe bloom in the post-extinction oceans. If so, microbes should be
62 widespread in various habitats, and occur in different forms in other facies (e.g.,
63 mudstone successions).
64 To test the model of Chen and Benton (2012), we examined the existence of
65 microbes in mudstone facies successions deposited immediately after the PTB mass
66 extinction in South China. Recently, we found abundant small microbialites from
67 calcareous mudstones located slightly above the PTB at the Tieshikou section,
68 southern Jiangxi Province, South China (Fig. 1A). The newly found small
69 microbialite offers additional material that reveals geobiologic features of the PTB
70 microbialites, and provides a better understanding of the accretion processes and
71 biogenic mechanisms of calcimicrobes and their proliferation in various
72 paleoenvironmental settings following the PTB biocrisis. Abundant ammonoids,
73 gastropods, ostracodes, and foraminifers are also found in association with the small
74 microbialite, further confirming that the metazoans associated with the microbialite

75 are more diverse than previously thought (Yang et al., 2011, 2015a, b; Forel, 2014;
76 Forel, et al., 2015).
77
78 **2. Geologic and stratigraphic settings**
79
80 The South China block was located near the equator in the eastern Paleo-Tethys
81 during the Permian−Triassic (P−Tr) transition; a massive, shallow carbonate platform,
82 the Yangtze Platform, extended from west to east across the South China block (Feng
83 et al., 1997; Ziegler et al., 1998). The western part of the platform is referred as the
84 Upper Yangtze Platform, while the eastern part is termed the Lower Yangtze Platform
85 (Sun et al., 1989; Fig. 1B). The Tieshikou section was situated at the junction between
86 the southeastern margin of the Lower Yangtze Platform and a shallow siliciclastic sea
87 to the southeast (Fig. 1B). The lower part of the section is made up of massive
88 bioclastic limestone of the uppermost Permian Changxing Formation, and the upper
89 part of the section is comprised of siliciclastics of the the lowermost Triassic
90 Tieshikou Formation (Fig. 2).
91 The Changxing Formation is made up of massive bioclastic limestone and
92 represents a shallow platform depositional environment, in which bioherms and
93 patchy sponge reef buildups are commonly present. This formation contains a diverse
94 assemblage of open marine biotas: foraminifers, dasycladacean algae, crinoids,
95 echinoids, articulate brachiopods, bivalves, gastropods, calcareous sponges, rugose
96 corals, and bryozoans (Ma, 2016). In particular, calcareous sponges include large,
97 complex, chambered sphinctozoan forms and form bioherms that are pronounced in
98 the field (Sun, 1988; Zhu et al., 1994). The *Clarkina yini* conodont Zone and the
99 *Palaeofusulina sinensis* fusulinid Zone, characteristic of late Changhsingian faunas of

South China (Sheng et al., 1984; Chen et al., 2015), are established from the uppermost Changxing Formation (Sun, 1988; Ma, 2016). The Tieshikou Formation is dominated by calcareous mudstone interbedded with muddy limestone layers and calcareous nodules, and represents a subtidal habitat (below fair-weather wavebase) within relatively deep siliciclastic shallow sea setting. The conodont *Hindeodus* cf. *parvus* was reported from a thin, muddy limestone layer, 0.5 m above the top of the Changxing Formation (Zhu et al., 1999; Wu et al., 2003). The calcareous mudstone of the basal Tieshikou Formation yields *Claraia* spp. bivalves, and the ammonoids *Hypophiceras* sp., *Lytophiceras* sp., and *Ophiceras* sp. (Sun, 1988; Zhu et al., 1994; Fig. 2). The small microbial buildup is preserved as limestone nodules embedded in three mudstone layers within the basal Tieshikou Formation (Fig. 3A−C). Associated metazoans include micro-gastropods, ostracodes, and the foraminifer *Earlandia* sp. (Fig. 2).

The presence of *H.* cf. *parvus* marks the PTB in Tieshikou (Zhu et al., 1994; Wu et al., 2003). This age assignment is also strengthened by the presence of *Claraia* sp., *Hypophiceras* sp., *Lytophiceras* sp., and *Ophiceras* sp. from the same horizons. The latter all occur in Beds 26−29 of the GSSP Meishan section, Changxing county, Zhejiang Province, South China (Yin et al., 2001; Chen et al., 2009, 2010, 2015), and are characteristic of the macrofaunas within the interval spanning the *Hindeodous changxingensis* to *Isarcicella staeschei* conodont zones in Meishan (Chen et al., 2015). The new calcimicrobial nodules therefore are earliest Griesbachian in age, and contemporaneous with widespread PTB microbialites from South China.

3. Material and methods

A total of 54 oriented samples were collected, slabbed, and thin-sectioned using conventional petrologic techniques. All thin sections were observed under the objective lens of a Leica DM2500P Microscope. A SU8010 FESEM equipped with EDS was also employed to observe thin sections and diagnose the mineral composition of the microbialites. Cathodoluminescence (CL) analyses were carried out on polished, uncovered thin sections with a Leica DM2500 Polarization Microscope with a Cambridge Image Technology (CITL) 8,200 Mk5 cold cathode instrument. This equipment is operated at a beam voltage of 12 kV and current of 198 uA. All images were produced under sufficient exposure times.

Some of suspected microbialite samples were etched with 1 % acetic acid for 5 min and submerged in distilled water to clear away residue attached to the surfaces. Samples were prepared for SEM examination by coating with platinum prior to SEM imaging and EDS analysis. All equipments are housed and analyses carried out at the State Key Laboratory of Biogeology and Environmental Geology, China University of Geosciences (Wuhan).

A micro drill was employed to obtain samples of microbialites for $\delta^{13}C_{carb}$ analysis. The sample powder was reacted offline and under vacuum with 100 % H_3PO_4 for 24 h at 25 °C. The carbon isotope composition of the generated CO_2 was measured using a Finnigan MAT 251 mass spectrometer. All isotopic data are reported as per mil (‰) relative to the Vienna Pee Dee belemnite (V-PDB) standard. The laboratory standard used for carbonate carbon and oxygen isotope compositions is TB-1 ($\delta^{13}C$ = 1.61 ‰, $\delta^{18}O$ = –11.59 ‰ relative to VPDB). The analytical precision is better than ± 0.1 ‰ for $\delta^{13}C$ and ± 0.2 ‰ for $\delta^{18}O$ based on duplicate analyses.

4. Results

150

151 *4.1. Mega-, macro- and meso-structures*

152

153 The basal Triassic calcareous mudstones with bowl-like nodules overlie Permian
154 limestones. A few bowl-like nodules occur in at least three calcareous mudstone
155 layers, 0.2 m, 0.6 m, and 0.7 m above the PTB, respectively (Fig. 3A). The bowl-like
156 nodules are elliptical on the top and hemispherical in profile (Figs 3−4). The
157 bowl-shaped structure contrasts with the surrounding calcareous mudstone (Fig. 3C);
158 laminations in the muddy host sediments are deflected around the nodules. The largest
159 nodule is up to 17 cm × 24 cm × 12 cm, and the smallest is 10 cm × 8 cm × 5 cm.

160 The bowl-shaped structures are clearly made up of the branching forms (Fig.
161 4A−C), which have a sharp contact with surrounding micritic sediments (Fig. 5B−C).
162 Dark colored columns, 1−5 mm wide and 10−12 cm high, are pronounced in profile;
163 all columnar branches point towards the bedding surface, indicating growth position.
164 The branches resemble mini-stromatolites, and are laminated and embedded within
165 grey micrite (Fig. 4A−C). In plane view, most of the dark colored branches are patchy
166 or strip-shaped, with a clotted structures (Fig. 4D), resembling that of a thrombolite.
167 The long axis of the branches is orientated to be perpendicular to bedding surface, and
168 most branches radiate from the center core towards the top of the bowl-like structure
169 (Fig. 4D). Some discrete spheroids show a structure that consists of
170 concentrically-stacked hemispheroids, 0.5−1.0 cm in diameter (Fig. 4E).

171 Clotted macrofabrics are prominent on polished blocks, and are comparable to
172 those of thrombolites (Fig. 5). Laminations are also occasionally visible in
173 macrofabrics in the vertical position. Except for the dark-colored, clotted fabrics, the
174 microbialite block also contains abundant ammonoid shells that are mainly distributed

along the outer margins of the microbialite (Fig. 5C) and occasionally scattered within clotted fabrics (Fig. 5B).

Most columns are cylindrical (Figs 6, 7A−D) or dendritic in outline (Fig. 7E−F); others are cotton-like (Fig. 7G−H), or cabbage-shaped (Fig. 7K−L). Moreover, some columns are composed of 2−3 smaller columns (Fig. 7A−B). Dissolution boundaries are pronounced between the microbialite and surrounding micritic sediments (Fig. 7H, J).

4.2. Microstructure

In petrographic thin section, the dark colored, branching columns are primarily made up of sparry calcite; clay minerals surround the branches. Ammonoids, micro-gastropods, ostracodes, and foraminifers (*Earlandia* sp.) are found within dark colored micrites, which make up the matrix surrounding the microbialites. Of these, ammonoids are commonly present at the top of the bowl-like structures.

The microbialite is comprised of columnar forms and fan-shaped structures (Figs 7−8). The columnar structures grow on carbonate precipitate fans and *vice versa* (Fig. 7A−B). One or more cement fans (~2 mm in width) are commonly found to grow from the outermost area of individual columns (Fig. 7C−F). Radial fibrous structures are distinct in both columns and fans (Fig. 7G−H). Pyrite particles are randomly distributed along the margins of cement fans or scattered on the dark-colored laminae of cement fans (Figs 7G−H, 8A). Pyrite crystals show octahedral or cubic morphologies in SEM images (Fig. 12B). The bases of the columns are circular (1−3 mm in diameter) (Fig. 7G−J).

Laminae are pronounced in most columns and cement fans, and consist of an

200 alternating ~0.1 mm wide dark colored layer and a ~0.5 mm wide light colored layer
201 (Fig. 7). Most laminae are arched, with arcs directed upwards. Radiating structures are
202 clustered to form features that are interpreted here as trichomes and are aligned
203 perpendicular to concentric laminae within columns and cement fans (Figs 7G−H, 8A,
204 D).

205 EDS element maps of the columns show high amounts of Silicon (Si), along with
206 aluminum (Al), oxygen (O), and magnesium (Mg) in the micrite, and high amounts of
207 calcium (Ca) in the columns (Fig. 9B−C). The dark colored laminae contain high Si
208 and Al contents, indicating a clay source (Fig. 9B). The laminae and fibrous fabrics
209 contain similar amounts of Si and Al in the EDS element maps. These
210 micro-structures are also pronounced in CL images of the columnar structures (Fig.
211 8A, 8D). Except for radiating structures, the columns also possess some bright, bent
212 calcite structures with dark edges that are distinct in CL images (Fig. 8A, 8D).

213

214 *4.3. Ultra-structures*

215 The dark colored lamina contain micrites, which demonstrate clay mineral (Al, O)
216 signatures in EDS analysis (Fig. 10C). The microbialite is surrounded by layers of
217 micrite (Fig. 12A). The micrite is made up of small particles that contain elevated
218 levels of Mg (Figs. 9C, 10C), indicating the presence of dolomite in the micrite
219 coatings. Nano-sized particles within columns (Fig. 10D) are interpreted to represent
220 calcified extracellular polymeric substances (EPS). These nano-sized carbonate
221 crystals irregularly interweave to form networks (Fig. 10D) that contain pronounced
222 rounded intraparticle pores, 1−2 μm in diameter (Fig. 10E). These micro-pores are
223 surrounded by walls made up of a mixture of calcium carbonate and silicates (Fig.
224 10D−E).

225 Rod-shaped filamentous structures, which form fibrous fabrics in CL images, are
226 also commonly present in sparry calcites of columnar structures within the
227 microbialites (Fig. 11A−D). Individual rods are straight to slightly curved in outline,
228 and range from 4−10 μm in diameter. EDS analysis shows that the Ca content is
229 pronounced. Some rods are solid, with smooth surfaces with a concave end in cross
230 section (Fig. 11C−F); others possess corroded surfaces (Fig. 11G−H) and 6−10
231 pronounced micropores in cross section (Fig. 11F, 11J−L). Single micropores are ~
232 0.5−1 μm in diameter (Fig. 11K−L).
233 Dolomite is also present in the microbialite as rhombohedral crystals (Fig. 12D),
234 which are frequently corroded on surfaces and near the margins (Fig. 12F−H). Some
235 are strongly corroded, with only the diamond shape remaining (Fig. 12H−I).
236 Filamentous sheaths (Figs 11I, 12G−I) and fossilized biofilms (Fig. 12E) are present
237 on the corrosion surfaces and probably represent calcified extracellular polymeric
238 substances (EPS). These filamentous sheaths, 0.7−1.0 μm in diameter, are usually
239 curved and randomly distributed on the surfaces of dolomite crystals or extend
240 through the crystals (Fig. 12G, 12I).
241
242 *4.4. Carbon and oxygen isotopes and pyrite framboid analysis*
243
244 Powders of the three components defined here (laminae within the microbialite,
245 fan-shaped structures, and micrite surrounding the microbialites) were collected using
246 a micro-drill and analyzed for carbon and oxygen isotopes using the techniques of
247 McCrea (1950). All analytical results appear in Table 1. Laminae within the
248 microbialite yield $\delta^{13}C$ and $\delta^{18}O$ values of –0.54 − +0.07 ‰ and –8.16 − –7.68‰,
249 respectively. Both $\delta^{13}C$ and $\delta^{18}O$ values of the fan-shaped structures are –0.82 −

250 +0.02 ‰ and –8.23 − –8.16 ‰, respectively. Micrite surrounding the microbialites
251 has $\delta^{13}C$ and $\delta^{18}O$ values of –0.96 − –0.91 ‰ and –8.74 − –7.99 ‰, respectively. The
252 $\delta^{13}C$ values therefore are not significantly different among the three components, and
253 are also broadly similar to those previously published for lowermost Triassic
254 carbonate-siliciclastic mixed successions (cf. ~ +1.5 ‰ from Magaritz and Holser,
255 1991). $\delta^{18}O$ values, which are depleted in ^{18}O relative to unmetamorphosed
256 equivalents, probably reflect the low-grade metamorphism that affected the formation.
257 None of the samples obtained from the six horizons near the PTB (Fig. 2) in the
258 Tieshikou section contain pyrite framboids, which may indicate oxic conditions (Bond
259 and Wignall, 2010), but it is important to note that pyrite needs sufficient iron, sulphur
260 and organic matter to form, and the lack of framboids is not an absolute indicator of
261 oxygenated conditions.
262
263 **5. Discussion**
264
265 *5.1. Difference between the small microbialite and red algae*
266
267 The Tieshikou section microbialite bears a remarkable resemblance to calcite
268 crusts described from the Late Neoproterozoic. The latter have been interpreted as the
269 remains of coralline red algae (Grant et al., 1991); red algae are commonly present in
270 Triassic successions (Flügel and Senowbari-Daryan, 2001), strengthening the
271 identification of red algae from the Tieshikou section. However, the microbialite
272 differs clearly from red algae based on a lack of outer walls. In contrast, Tieshikou
273 section microbialite possesses pronounced laminae and very faint radial structures.
274 Moreover, the Tieshikou microbialite is also characterized by conspicuous fan-shaped

branches (Fig. 7), which are significantly different from red algae branches; in the microbialite, amorphous branches grow above the older branches (Fig. 7). The Permian red alga *Solenopora* described by Wu (1991) from the Longlin area, Guizhou, South China possesses radiating filaments with prominent walls, which resemble radial structures of Tieshikou section microbialite. The latter, however, are very faint and overlapped with distinct laminae, and never form filaments, as observed in red alga *Solenopora* (Wu, 1991). Moreover, pyrite particles are dispersed in the microbialite, similar to those seen in other PTB microbialites (Wang et al., 2005; Liao et al., 2010; Yang et al., 2011), but rarely present in red algae.

5.2. Taphonomy and geobiologic process associated with accretion of the microbialite

The nodular morphology and occurrence of widespread PTB microbialites in carbonate platform settings in South China suggest that the bowl-like microbialite may have been transported from the adjacent platform and re-deposited in the siliciclastic setting of the Tieshikou section. Although PTB microbialites have been reported from 38 sites across South China, they are rare in the Lower Yangtze platform (Wu et al., 2017). The closest known PTB microbialite site is located in the Xiushui area, ~400 km north of the Tieshikou section (Wu et al., 2017; Fig. 1). In addition, ammonoid fossils are unique to the Tieshikou microbialite, and have never been found in any known PTB microbialites in South China (Yang et al., 2008, 2011; Kershaw et al., 2012; Adachi et al., 2017; Fang et al., 2017). More importantly, all microbialite columnar branches within the bowl-shaped structures point towards the bedding surface, indicating an upright growth position (Fig. 4A−C). This also indicates that the microbialites are in place and have not been transported. Horizontal

300 laminae in surrounding mud sediments are deflected around the nodules (Fig. 3C),
301 indicating syn-deposition of nodule with surrounding sediments. Thus, the bowl-like
302 structures are *in situ* and are not transported.

303 The Tieshikou section microbialite resembles amalgamated structures of
304 stromatolites and crystal fans reported from the Cambrian and Carboniferous to
305 Pleistocene strata (Riding, 2000, 2008, 2011). Of these, Cambrian and Carboniferous
306 fine-grained stromatolitic crusts possess uneven to discontinuous, poorly defined
307 layers (Riding, 2011, figs. 5, 18). Similar characteristics are also observed in the
308 Tieshikou microbialites (Figs. 4−6). The small stromatolites exhibit uneven to
309 discontinuous (Fig. 4), poorly defined layers (Fig. 6). Moreover, microfabrics of
310 fine-grained stromatolitic crusts from Carboniferous and Pleistocene strata show
311 dense, clotted, peloidal, and/or filamentous morphologies (Riding, 2000, figs. 5−7),
312 are dominated by micrite and microspar and may contain fenestrae and allochthonous
313 grains (Riding, 2000, 2011). The Tieshikou radiating cement fans do not show all
314 microfabric morphologies of stromatolitic crusts mentioned above, but do possess
315 dark, laminated layers that contain allochthonous clay minerals (Fig. 9). To sum up,
316 the amalgamation of stromatolitic crusts and crystal fans from the Tieshikou
317 microbialite share many features with Phanerozoic fine-grained stromatolitic crusts:
318 both have microfabric and irregular or poorly-layered macrofabrics that are suggestive
319 of a biogenic origin (Riding, 2011).

320

321 *5.2.1. Laminated columns*

322 All columns of the Tieshikou microbialite possess laminar structures that exhibit
323 alternating dark and bright layers within columns. The columnar laminae exhibit
324 similar characteristics as those of modern marine stromatolites. The thin micrite layers

of modern stromatolites are interpreted to be the result of bacterial activity (Visscher et al., 2000; Dupraz et al., 2004, 2009; Dupraz and Visscher, 2005), and also contribute to the formation of the laminated fabric (Arp et al., 1999a, b, 2001, 2003; Reid et al., 2000). SEM imaging of stromatolites from Shark Bay, Western Australia shows that the dark-colored layers are comprised of polyhedral clay aggregates, which are interpreted to form as the result of a benthic microbial community (BMC) trapping and binding detrital sediment and/or forming the locus of mineral precipitation (Reid et al., 2000). Similar clay aggregates are also observed within the columnar structures of the Tieshikou microbialite (Fig. 9B–C). The Tieshikou laminated columns are therefore thought to be biogenic.

5.2.2. Fibrous fabrics in cement fans

Carbonate precipitates (also termed seafloor fans, Woods et al., 1999) comprised of radiating calcite crystals have been frequently reported from Lower Triassic successions worldwide (Woods et al., 1999, 2007; Baud et al., 2007; Woods and Baud, 2008). Syn-sedimentary cements also occur within some Lower Triassic microbialites (Baud et al., 2007; Kershaw et al., 2007, 2011; Lehrmann et al., 2015). A lack of similar microbial features in association with seafloor carbonate precipitates from other regions points to an abiotic origin, although it is impossible to exclude the possibility that microbes may have played a role in their formation (Woods, 2014). In contrast, some biogeochemical signals mirroring various microbial communities associated with benthic microbial mats have been detected from diagenetic carbonate crystal fan deposits of Dienerian-Smithian age (Heindel et al., 2014). Microbial fossils within cements from Oman provide more robust evidence of a microbial influence during cement growth (Woods and Baud, 2008; Woods, 2014).

When compared with the Tieshikou cement fans, all known synsedimentary cements are slightly different in having radiating calcite crystals (Woods et al., 1999, 2007; Woods and Baud, 2008), and lacking concentric laminae and pyrite crystals, which are observed in the Tieshikou precipitate fans (Fig. 7). In contrast, both concentric laminae and radial fibrous fabrics (also trichome-like structures) (Fig. 8A, D) characterize the Tieshikou cement fans, which usually exhibit 3−5 concentric laminae and densely arranged, neatly aligned trichomes. The latter are often perpendicular to the concentric laminae (Fig. 7). Similar micro-structures have also been reported from the Frasnian succession at the Lion quarry of Frasnes, Belgian Ardennes (Monty, 1995). These Devonian micro-structures are interpreted as flagellates and the finely laminated structures are reminiscent of the modern cyanophyte *Rivularia* (Monty, 1995), although the latter is almost always found as a freshwater cyanobacterium (Kershaw and Guo, 2003, 2006; Antonioli et al., 2006; Andrews et al., 2007).

Concentric laminae and radial trichomes are also observed in the modern *Rivularia haematites* stromatolite (Caudwell et al., 2001), which are similar to the texture of the Tieshikou cement fan structures. The growth of the *Rivularia* stromatolite is interpreted to reflect a wide range of biological, environmental, and climatic factors (Caudwell et al., 2001). Concentric laminae could be the result of microbial growth, while cement growth is coupled to the growth of the radial trichomes (Caudwell et al., 2001). Accordingly, both biological and sedimentary processes are crucial for the accretion of these unique micro-structures.

The rod-like aggregates of the Tieshikou cement fans also share many common characteristics with present-day *Rivularia* structures (Caudwell et al., 2001). Micropores that occur within a single rod, which are prominent in the Tieshikou

375 samples (Fig. 11K−L), are also observed in the trichomes of present-day *Rivularia*
376 *haematites* stromatolites, and are interpreted to represent honeycomb structures found
377 in transverse sections *Rivularia* stromatolite filaments (Caudwell et al., 2001, fig. 8).
378 In addition, the rods of the Tieshikou microbialite share a similar size and
379 interweaving pattern with fossilized cyanobacteria filaments from the literature
380 (Golubic et al., 2000; Seong-Joo et al., 2000) and to modern stromatolites from
381 hypersaline lakes (Kaźmierczak et al., 2011). Accordingly, the Tieshikou microbialite
382 is highly similar to *R. haematites*, and thus exhibits many features of a
383 cyanobacterium. If so, these putative fossilized bacterial filaments may represent the
384 primary producers that constructed the Tieshikou microbialite.
385
386 *5.2.3. Biogenicity recorded in nano-sized structures*
387 Three types of nano-sized structures from the Tieshikou microbialite indicate
388 biogenicity, including intraparticle micropores, fibrous biofilms, and filamentous
389 sheaths. The first type structure occurs in the networks woven by nano-sized calcium
390 carbonate crystals within a micritic matrix (Fig. 10D−E). Fibrous biofilms are
391 frequently seen within dolomite crystals (Fig. 12E), and nano-sized filamentous
392 sheaths are abundant on the surfaces of and within dolomite crystals (Fig. 12G−I).
393 Intraparticle micropores often occur within the micritic matrix (Fig. 10D−E) of
394 both the laminated columns and the radiating cement fans of the Tieshikou
395 microbialite, and are distributed throughout the crystals as opposed to being zoned
396 and limited to the crystal edges. The intraparticle micropores share many features
397 with other biogenic micropores observed in modern and ancient stromatolites, except
398 for a slightly smaller size (Bosak et al., 2004), and are thus also interpreted as an
399 indication of a microbial signature.

Irregular, but mostly fibrous biofilms frequently are seen in the dolomite crystals when their surfaces are corroded (Fig. 12E). Similar fibrous filaments have also been reported from the dolomite-precipitating environment of a Miocene lacustrine system, and are interpreted to be the residue of extracellular polymeric substances (EPS) (Sanz-Montero et al., 2008). Fibrous biofilms are also commonly present in modern and fossilized stromatolites and microbial mats (Arp et al., 1999a, b, 2001; Noffke et al., 2003; Dupraz et al., 2004, 2009; Dupraz and Visscher, 2005; Shiraishi et al., 2008; Noffke, 2010; Glunk et al., 2011; Luo et al., 2013, 2014; Chen et al., 2014; Neu and Lawrence, 2015; Ionescu et al., 2015; Tu et al., 2016; Xu et al., 2017; Decho and Gutierrez, 2017). Morphologically, the Tieshikou fibrous biofilms are strong evidence of fossilized EPS, however, whether these nano-sized microstructures obtained from geological samples can be compared directly to modern EPS remains to be determined (Arp et al., 2001; Shiraishi et al., 2008; Dupraz et al., 2009; Neu et al., 2010; Glunk et al., 2011; Neu and Lawrence, 2015; Ionescu et al., 2015; Decho and Gutierrez, 2017). This is because few studies have revealed how diagenesis affects the lithification of EPS from living objects to fossilized forms. Thus, the assignment of the Tieshikou nano-sized particles to fossilized EPS is rather tentative, and needs to be confirmed by future work on the effects of diagenesis on nano-sized biogenic structures.

Linear sheaths are also frequently found in corroded dolomite crystals within the Tieshikou microbialite (Fig. 12F−G). These linear, hollow tubes resemble microboring traces that can be identified to the ichnospecies level, including *Eurygonum nodosum*, a trace forming a branched meshwork of 6 to 10 μm thick galleries with diagnostic short swollen apophyses, and presumably produced by the filamentous hetroscystous cyanobacterium *Mastigocoleus testarum* (Glaub et al.,

425 2007). However, these tiny tubes are unlikely to be endoliths that are produced by
426 rock-eating bacteria due to their small size (usually 0.5−1 μm in diameter). In contrast,
427 these sheaths are almost identical to the residues of modern bacterial sheaths (in size
428 and shape) that are observed from Lagoa Vermelha (Lith et al., 2003). They also
429 could be the residues of sulphate-reducing bacteria that have been reported from strain
430 LVform6 from modern cultures and are closely related to dolomite dumbbells (Lith et
431 al., 2003). Accordingly, the Tieshikou nano-sized sheaths bear a remarkable
432 resemblance to the moulds of bacteria that form during the precipitation of dolomite
433 crystals. However, several observations of modern microbialites or microbial mats
434 show that similar microbial filaments could have many origins and are not restricted
435 to cyanobacteria (Arp et al., 1999a, b, 2001; Shiraishi et al., 2008; Dupraz et al., 2009;
436 Ionescu et al., 2015; Decho and Gutierrez, 2017). Additional work is needed to clarify
437 the origin of these features.
438
439 *5.3. Comparisons with other Early Triassic microbialites*
440
441 Although Early Triassic microbialites have been globally reported, detailed
442 geomicrobiologic analysis of these unusual deposits has largely lagged behind the
443 study of their ecologic significance (Chen et al., 2017), although some detailed works
444 have been conducted. The PTB stromatolites from the Bükk Mountains of Hungary
445 yield abundant microstructures such as spheroid clusters, aggregates of micrite clots,
446 and bundles of prostrate micrite threads (Hips and Haas, 2006). These authors
447 interpret the spheroids to be calcified coccoid cyanobacteria. Yang et al. (2011)
448 describe a stromatolite from the Chongyang PTB section of southern Hubei Province,
449 South China. In addition to *Renalcis*-like structures found in stromatolitic laminae

(Wang et al., 2005), the Chongyang stromatolite is also dominated by coccoid bacteria (Yang et al., 2011). Other PTB and Early Triassic stromatolites have also been reported from around the world (e.g., Pruss et al., 2006; Baud et al., 2007; Kershaw et al., 2011, 2012). However, their microbial composition remains unclear because no geobiologic studies have been undertaken.

Macroscopic features of the Tieshikou microbialites are very similar to those of some PTB thrombolites. However, the Tieshikou microbialites possess laminated structures among coarse grains, whereas other PTB thrombolites have sparitic structures composed of coarse grains. Kershaw et al. (2007) interpreted these sparitic structures within the PTB thrombolites to be altered microbes that have a "*Renalcis*-like" character, but is actually is different from *Renalcis*, so there is no clarity as to the nature of the microbes. Alternatively, Wu et al. (2014, 2016) interpret the same structures as colonies of microbial organisms comparable to the modern cyanobacterium *Microcystis*. However, their identification of *Microcystis* is also questionable because bacterial colonies occur on vertical rock walls of the Laolongdong microbialite, which span a stratal interval of several centimeters in thickness. The compaction and deformation of microbialite sediments after lithification and diagenesis prevent the direct comparison of the imprinted bacterial colonies on microbialites to modern-day planktic *Microcystis* colonies (Luo et al., 2016a; Fang et al., 2017).

Filamentous fossils are often found in digitate microbialites and aragonite fans beneath the PTB microbialites in South China (i.e. Lehrmann et al., 2015, fig. 8C−D). Similar microfossils are also reported from other PTBMs in South China (Wang et al., 2005; Yang et al., 2011). The filamentous fossils are thought to be major builders of microbialites (Wang et al., 2005; Yang et al., 2011), although they are absent from the

475 Tieshikou microbialite. Aragonite crystal fans are extensively recrystallized but retain
476 a fine acicular habit and square-tipped crystal terminations, typical of marine
477 aragonite (Lehrmann et al., 2015).
478
479 *5.4. Implications for post-extinction marine conditions in siliciclastic shallow seas*
480
481 Widespread PTB microbialites are usually interpreted as an unusual
482 biosedimentary phenomenon related to the severe PTB mass extinction and its
483 consequences (Kershaw et al., 2012). The microbial composition of several Lower
484 Triassic stromatolites was largely controlled by inhospitable anoxic/sulphidic marine
485 conditions that prevailed in the oceans during that time (Ezaki et al., 2008, 2012;
486 Saito et al., 2014; Luo et al., 2016a). Biogeochemical signals also show that microbes
487 are indeed extremely abundant immediately after the end-Permian extinction, even in
488 microbialite-free carbonate settings such as Meishan, South China (Xie et al., 2005).
489 Thus, microbes existed widely in various niches of carbonate environments after the
490 PTB extinction. However, whether microbes also proliferated in marine siliciclastic
491 habitats immediately after the PTB extinction still remains unclear.
492 Kershaw et al. (2007) and Woods et al. (2007) also emphasized that elevated
493 carbonate supersaturation caused by the upwelling of $CaCO_3$-rich anoxic waters,
494 mixed with aerated surface waters, may be the key driver for the precipitation of the
495 PTB microbialites. Nevertheless, Kershaw et al. (2012) point out that the poor
496 representation of seafloor cements in post-extinction facies in South China reduces
497 the likelihood of supersaturation as a major control on microbialite formation. The
498 saturation issue is a complex one, not least because of the highly saturated carbonate
499 conditions expected in the post-extinction oceans (Grotzinger and Knoll, 1995; Woods

et al., 1999; Riding and Liang, 2005; Pruss et al., 2006; Riding, 2006; Baud et al., 2007) due to the loss of skeletal taxa increasing the availability of bicarbonate, combined with factors unfavorable to most normal skeletal organisms. Recent elemental and pyrite framboid analyses reveal that some PTB microbialites may also have been deposited under dysoxic conditions (Liao et al., 2010), yet Loope et al. (2013) present evidence for an oxygenated environment. Similarly, abundant and diverse ostracod, microconchid, and benthic faunas derived from PTB microbialites also indicate that the associated environments of PTB microbialites were neither anoxic nor inhospitable to shelly organisms (Forel et al., 2012; Forel, 2013; Yang et al., 2015a, b; Wu et al., 2017).

The Tieshikou fibrous carbonate precipitates share similar accretion process to PTB microbialites, and formed under a similar seawater chemistry to the PTB microbialites. Syn-sedimentary precipitation of calcium carbonate fans was mediated through rapid shifts in the chemistry of ambient waters. The microenvironment (e.g. Eh and pH) was changed due to microbial activity, and such an ambient environment may have stimulated the deposition of more microbial sediments (Heindel et al., 2014). Then, some laminated columns or micro-stromatolites grew along the carbonate precipitate fans (Fig. 13).

The Tieshikou microbialites are preserved in the form of nodules within mudstone. The PTB succession in Tieshikou represents an offshore environment (Zhu et al., 1994). The slightly negative carbon isotope values are derived from cement fans, microspars, and micrites of the Tieshikou microbialite (Table 1). All horizons examined here contain no pyrite framboids. Moreover, the micrite surrounding the microbialites yields ammonoids, microgastropods, ostracodes, and foraminifers. All lines of evidence suggest that the Tieshikou microbialite grew in an oxic marine

environment immediately after the end-Permian crisis. Surprisingly, contemporaneous siliciclastic or carbonate shallow seas were usually dyoxic to anoxic in South China (Chen et al., 2015; Li et al., 2016; Huang et al., 2017). Accordingly, the growth of the PTB microbialites appears to not be restricted by oxygen levels; instead PTB microbialites were affected by other seawater chemical conditions. Further work is necessary to test such an inference for oceanographic conditions during growth of the PTB microbialites.

5.5. Implication for the genesis of calcareous nodules in mudstone or nodular limestone of the Lower Triassic

Comparable compositions and geobiologic features to those of the PTB microbialites indicate that the Tieshikou microbialite could share similar biogenetic mechanisms to other microbialites. Abundant microbes and a highly saturated water mass could provide a hospitable environment for the growth of microbialites during the P−Tr transition.

Besides, the nodular preservational state resembles that of calcareous nodular mudstone or nodular argillaceous limestone, implying that these deposits may share similar biogenetic mechanism to that of Tieshikou microbialites. Nodular mudstone or argillaceous limestone is one of most widely distributed rocks within Lower Triassic successions in South China (Chen et al., 2011; Luo et al., 2016b; Fig. 2B). This implies that nodular mudstone or muddy limestone might also be deposited in a microbe-rich, highly saturated environment, although elevated terrigeneous supply immediately after the end-Permian crisis (Algeo and Twitchett, 2010; Zhao et al., 2013) may have modulated sedimentation in siliciclastic settings during that time. If

so, the nodular mudstone or muddy limestone is also likely of microbial origin, and they and represent an alternative forms of microbial preservation in Lower Triassic strata. However, further work is necessary to test biogenesis of Lower Triassic nodular mudstone and argillaceous limestone.

The Chen-Benton fossilized trophic pyramid model proposes that most primary consumers and higher trophic functioning structures collapsed as a result of the PTB mass extinction (Chen and Benton, 2012). As a consequence, a primary producer-dominated community (i.e., microbes) prevailed in the post-extinction oceans. However, such a microbial proliferation can only be identified from a few types of Lower Triassic sedimentary records, such as microbialites and microbially-induced sedimentary structures (MISSs) (i.e., Xu et al., 2017). Furthermore, microbialites only peaked during several short intervals (i.e. PTB, Griesbachian-Dienerian transition, early Smithian, late Smithian, and late Spathian; Baud et al., 2007; Chen et al., 2014; Luo et al., 2016a), and no sedimentary record shows microbialites across the duration of the Early Triassic.

The occurrence of microbialites in Lower Triassic mudstones implies that microbes were still abundant in post-extinction marine habitats, although they may be preserved in the form of nodules embedded within mudstone or argillaceous limestone, at least in South China (Luo et al., 2016b; Fig. 2B), supporting the scenario of a microbial proliferation in post-extinction oceans (Chen and Benton, 2012).

6. Conclusions

A new type of microbialite is described from the nodular mudstones just above the P−Tr boundary at the Tieshikou section, southern Jiangxi Province, South China.

575 The microbialite occurs as a bowl-like structure that displays densely laminated
576 stromatolitic columns in profile and clotted thrombolite textures in plane view.
577 Radiating cement fans contain concentric laminae and pronounced fibrous fabrics,
578 resembling seafloor carbonate precipitates. Under SEM, the radiating fans are
579 represented by rod-shaped filaments, which are interpreted as calcified
580 trichomes/filaments. Prominent micropores within rods represent the multiple sheaths
581 of false branching zones of trichomes. Thus, both the columns and radiating fans are
582 probably microbial in origin. Moreover, three types of nano-sized structures:
583 intraparticle micropores, fibrous biofilms, and filamentous sheaths are also recognized
584 from the Tieshikou microbialite, and all strongly indicate biogenicity. In particular,
585 the well-preserved fibrous biofilms could represent fossilized EPS, and worm-like
586 sheaths are interpreted as the residues of bacteria that formed during the precipitation
587 of dolomite crystals. These two nano-sized structures are associated with dolomite
588 crystals, suggesting that dolomite in the Tieshikou microbialite is microbial in origin.
589 The geobiologic features of the Tieshikou microbialite resemble those of the
590 widespread microbialites that occur near the P–Tr boundary, suggesting both share
591 similar accretion mechanisms and depositional environments. The combination of an
592 absence of pyrite framboids, slightly negative carbon isotope values, and an
593 association with fairly abundant ammonoids, bivalves, and gastropods indicates oxic
594 conditions during growth of the Tieshikou microbialite. Accordingly, the Tieshikou
595 microbialite is indicative of a microbial bloom that not only occurred in shallow
596 carbonate habitats, but also extended to relatively deep siliciclastic offshore settings
597 after the end-Permian mass extinction. Moreover, the comparable diagenetic state of
598 the microbialite with that of the widespread nodular mudstone or muddy limestone of
599 the Lower Triassic successions implies that abundant microbes may have also existed

600 in the Early Triassic oceans even if microbialites are not found.

601

602 **Acknowledgments**

603 We are grateful to both Robert Riding and Judith Mackenzie for their advices on
604 the genesis of some micro-structures during drafting the paper. Critical comments and
605 constructive suggestions by three anonymous reviewers and guest editor Shane
606 Schoepfer have improved greatly the quality of the paper. This study was supported
607 by three NSFC research grants (41572091, 41772007, 41661134047), one Hubei
608 Provincial Natural Science Foundation grant (2017CFA019), and the Fundamental
609 Research Funds for the Central Universities, China University of Geosciences
610 (Wuhan). It is a contribution to IGCP 630.

611

612 **References**

613 Arp, G., Reimer, A., Reitner, J., 1999a. Calcification in cyanobacterial biofilms of
614 alkaline salt lakes. European Journal of Phycology 34, 393–403.

615 Arp, G., Thiel, V., Reimer, A., Michaelis, W., Reitner, J., 1999b. Biofilm
616 exopolymers control microbialite formation at thermal springs discharging into the
617 alkaline Pyramid Lake, Nevada, USA. Sedimentary Geology 126, 159–176.

618 Arp, G., Reimer, A., Reitner, J., 2001. Photosynthesis-induced biofilm calcification
619 and calcium concentrations in Phanerozoic oceans. Science 292, 1701–1704.

620 Adachi, N., Adachi, Y., Adachi, Y., Liu, J.B., 2017. Stromatolites near the
621 Permian-Triassic boundary in Chongyang, Hubei Province, South China: A
622 geobiological window into palaeo-oceanic fluctuations following the end-Permian
623 extinction. Palaeogeography, Palaeoclimatology, Palaeoecology 475, 55−69.

624 Algeo, T.J, Twitchett, R.J., 2010. Anomalous Early Triassic sediment fluxes due to

625 elevated weathering rates and their biological consequences. Geology 38,
626 1023−1026.
627 Andrews, J.E., Leeder, M.R., Portman, C., Rowe, P.J., Smith, S., Kershaw S., Guo, L.,
628 2007. Discussion on Pleistocene calcified cyanobacterial mounds, Perachora
629 peninsula, central Greece: a controversy of growth and history. Journal of the
630 Geological Society 164, 1065−1072.
631 Antonioli, F., Kershaw, S., Renda, P., Rust, D., Belluomini, G., Cerasoli, M., Radtke,
632 U., Silenzi, s., 2006. Elevation of the last interglacial highstand in Sicily (Italy): a
633 benchmark of coastal tectonics. Quaternary International 145−146, 3−18.
634 Bagherpour, B., Bucher, H., Baud, A., Brosse, M., Vennemann, T., Martini, R.,
635 Goudun, K., 2017. Onset, development, and cessation of basal Early Triassic
636 microbialites (BETM) in the Nanpanjiang pull-apart Basin, South China Block.
637 Gondwana Research 44, 178–204.
638 Baud, A., Richoz, S., Pruss, S.B. 2007. The Lower Triassic anachronistic carbonate
639 facies in space and time. Global and Planetary Change 55, 81−89.
640 Bond, D.P., Wignall, P.B., 2010. Pyrite framboid study of marine Permian−Triassic
641 boundary sections: a complex anoxic event and its relationship to
642 contemporaneous mass extinction. Geological Society of America, Bulletin 122,
643 1265−1279.
644 Bosak, T., Souza-Egipsy, V., Corsetti, F.A., Newman, D.K., 2004. Micrometer-scale
645 porosity as a biosignature in carbonate crusts. Geology 32, 781−784.
646 Caudwell, C., Lang, J., Pascal, A., 2001. Lamination of swampy-rivulets Rivularia
647 haematites stromatolites in a temperate clamate. Sedimentary Geology 143,
648 125−147.
649 Chen, Z.Q., Benton, M.J., 2012. The timing and pattern of biotic recovery following

650 the end-Permian mass extinction. Nature Geosciences 5, 375−383.
651 Chen, Z.Q., Tong, J., Zhang, K., Yang, H., Liao, Z., Song, H., Chen, J., 2009.
652 Environmental and biotic turnover across Permian−Triassic boundary from
653 shallow carbonate platform in western Zhejiang, South China. Australian Journal
654 of Earth Sciences 56, 775−797.
655 Chen, Z.Q., Tong, J.N., Liao, Z.T., Chen, J., 2010. Structural changes of marine
656 communities over the Permian−Triassic transition: ecologically assessing the
657 end-Permian mass extinction and its aftermath. Global and Planetary Change 73,
658 123−140.
659 Chen, Z.Q., Tong, J.N., Fraiser, M.L., 2011. Trace fossil evidence for restoration of
660 marine ecosystems following the end-Permian mass extinction in the Lower
661 Yangtze region, South China. Palaeogeography, Palaeoclimatology, Palaeoecology
662 299, 449−474.
663 Chen, Z.Q., Wang, Y.B., Kershaw, S., Luo, M., Yang, H., Zhao, L.S., Fang, Y.H.,
664 Chen, J.B., Li, Yang, Zhang, L., 2014. Early Triassic stromatolites in a siliciclastic
665 nearshore setting in northern Perth Basin, Western Australia: geobiologic features
666 and implications for post-extinction microbial proliferation. Global and Planetary
667 Change 121, 89−100.
668 Chen, Z.Q., Yang, H., Luo, M., Benton, M.J., Kaiho, K., Zhao, L.S, Huang, Y., Zhang,
669 K.X., Fang, Y., Jiang, H.S., Qiu, H., Li, Y., Tu, C.Y., Shi, L., Zhang, L., Feng,
670 X.Q., Chen, L., 2015. Complete biotic and sedimentary records of the
671 Permian−Triassic transition from Meishan section, South China: ecologically
672 assessing mass extinction and its aftermath. Earth-Science Reviews 149, 63−103.
673 Chen, Z.Q., Zhou, C., Stanley, G.J., 2017. Biosedimentary records of China from the
674 Precambrian to present. Palaeogeography, Palaeoclimatology, Palaeoecology 474,

675 1−6.
676 Decho, A.W., Gutierrez, T., 2017. Microbial Extracellular Polymeric Substances
677 (EPSs) in Ocean Systems. Frontiers in Microbiology 8, 922e doi:
678 10.3389/fmicb.2017.00922
679 Dupraz, C., Visscher, P.T., 2005. Microbial lithification in marine stromatolites and
680 hypersaline mats. Trends of Microbiology 13, 429–439.
681 Dupraz, C., Visscher, P.T., Baumgartner, L.K., Reid, R.P., 2004. Microbe-mineral
682 interactions: early carbonate precipitation in a hypersaline lake (Eleuthera Island,
683 Bahamas). Sedimentology 51, 745–765.
684 Dupraz, C., Reid, R.P., Braissant, O., Decho, A.W., Norman, S.R., Visscher, P.T.,
685 2009. Processes of carbonate precipitation in modern microbial mats.
686 Earth-Science Reviews 96, 141–162.
687 Ezaki, Y., Liu, J.B., Adachi, N., 2003. Earliest Triassic microbialite micro to
688 megastructures in the Huaying area of Sichuan Province, South China:
689 implications for the nature of oceanic conditions after the end–Permian extinction.
690 Palaeogeography, Palaeoclimatology, Palaeoecology 18, 388–402.
691 Ezaki, Y., Liu, J., Nagano, T., Adachi, N., 2008. Geobiological aspects of the earliest
692 Triassic microbialites along the southern periphery of the tropical Yangtze
693 Platform: initiation and cessation of a microbial regime. Palaeogeography,
694 Palaeoclimatology, Palaeoecology 23, 356–369.
695 Ezaki, Y., Liu, J.B., Adachi, N., 2012. Lower Triassic stromatolites in Luodian County,
696 Guizhou Province, South China: evidence for the protracted devastation of the
697 marineenvironments. Geobiology 10, 48−59.
698 Fang, Y.H., Chen, Z.Q., Kershaw, S., Yang, H., 2017. Permian−Triassic boundary
699 microbialites at Zuodeng Section, Guangxi Province, South China: geobiology

700 and palaeoceanographic implications. Global and Planetary Change 152,
701 115−128.
702 Feng, Z.Z., Bao, Z.D., Li, S.W., 1997. Lithofacies Paleogeography of Early and
703 Middle Triassic of South China. Petroleum Industry Press, Beijing, pp. 1−222 (in
704 Chinese).
705 Flügel, E., Senowbari-Daryan, B., 2001. Triassic reefs of the Tethys. In: Stanley, G.D.
706 (Ed.), The History and Sedimentology of Ancient Reef Systems. Kluwer
707 Academic Plenum, pp. 217−249.
708 Forel, M.B., 2013. The Permian−Triassic mass extinction: ostracods (Crustacea) and
709 microbialites. Comptes Rendus Geoscience 345, 203−211.
710 Forel, M.B., 2014. Heterochronic growth of ostracods (Crustacea) from microbial
711 deposits in the aftermath of the end-Permian extinction. Journal of Systematic
712 Palaeontology 13, 1-35.
713 Forel, M.B., Crasquin, S., Anisong, C., Lucia, A., Maurizio, G., 2015. Precocious
714 sexual dimorphism and the Lilliput effect in Neo-Tethyan Ostracoda (Crustacea)
715 through the Permian−Triassic boundary. Palaeontology, 1−46.
716 Forel, M.B., Crasquin, S., Kershaw, S., Collin, P.Y., 2012. In the aftermath of the
717 end-Permian extinction: the microbialite refuge? Terra Nova 25, 137−143.
718 Friesenbichler, E., Richoz, S., Baud, A., Krystyn, L., Sahakyan, L., Vardanyan, S.,
719 Peckmann, J., Reitner, J., Heindel, K., 2018. Spong-microbial build-ups from the
720 lowermost Triassic Chanakhchi section in southern Armenia: microfacies and
721 stable carbon isotopes. Palaeogeography, Palaeoclimatology, Palaeoecology 490,
722 653−672.
723 Grant, S.W.F., Knoll, A.H., Germs, G.J.B., 1991. Probable calcified *Metaphytes* in the
724 latest Proterozoic Nama Group, Namibia: origin, diagenesis, and implications.

725 Journal of Paleontology 65, 1−18.
726 Glaub, I., Golubic, S., Gektidis, M., Radtke, G., Vogel, K., 2007. Chapter 21 -
727 Microborings and microbial endoliths: geological implications. In: Miller, W.
728 (Ed.), Trace Fossils. Amsterdam, Elsevier, pp. 368−381.
729 Glunk, C., Dupraz, C., Braissant, O., Gallagher, K.L., Verrecchia, E.P., Visscher, P.T.,
730 2011. Microbially mediated carbonate precipitation in a hypersaline lake, Big
731 Pond (Eleuthera, Bahamas). Sedimentology 58, 720–736.
732 Golubic, S., Seong-Joo, L., Browne, K.M., 2000. Cyanobacteria: architects of
733 sedimentary structures. In: Riding, R., Awramik, S.M. (Eds.), Microbial
734 Sediments. Springer-Verlag, Berlin-Heidelberg, pp. 57−67.
735 Grotzinger, J.P., Knoll, A.H., 1995. Anomalous carbonate precipitates: is the
736 Precambrian the key to the Permian? Palaios 10, 578−596.
737 Heindel, K., Richoz, S., Birgel, D., Brandner, R., Klugel, A., Krystyn, L., Baud, A.,
738 Horacek, M., Mohtat, T., Peckmann, J., 2014. Biogeochemical formation of
739 calyx-shaped carbonate crystal fans in the subsurface of the Early Triassic
740 seafloor. Gondwana Research 27, 840−861.
741 Hips, K., Haas, J., 2006. Calcimicrobial stromatolites at the Permian−Triassic
742 boundary in a western Tethyan section, Bükk Mountains, Hungary. Sedimentary
743 Geology 185, 239−253.
744 Huang, Y.G., Chen, Z.Q., Wignall, P.B., Zhao, L.S., 2017. Latest Permian to Middle
745 Triassic redox condition variations in ramp settings, South China: pyrite framboid
746 evidence. Geological Society of America, Bulletin 129, 229−243.
747 Ionescu, D., Spitzer, S., Reimer, A., Schneider, D., Daniel, R., Reitner, J., Beer, D. de,
748 Arp, G., 2015. Calcium dynamics in microbialite-forming exopolymer-rich mats
749 on the atoll of Kiritimati, Republic of Kiribati, Central Pacific. Geobiology 13,

170–180.

Kaźmierczak, J., Kempe, S., Kremer, B., López-García, P., Moreira, D., Tavera, R., 2011.Hydrochemistry and microbialites of the alkaline crater lake Alchichica, Mexico. Facies 57, 543−570.

Kershaw, S., Guo, L., 2003. Pleistocene cyanobacterial mounds in the Perachora Peninsula, Gulf of Corinth, Greece: structure and applications to interpreting sea-level history and terrace sequences in an unstable tectonic setting. Palaeogeography, Palaeoclimatology, Palaeoecology 193, 503−514.

Kershaw, S., Guo, L., 2006. Pleistocene calcified cyanobacterial mounds, Perachora Peninsula, central Greece: a controversy of growth and history. Cool-Water Carbonates: Depositional Systems and Palaeoenvironmental Controls 255, 53−69.

Kershaw, S., Zhang, T., Lan, G., 1999. A ?microbialite crust at the Permian–Triassic boundary in South China, and its palaeoenvironmental significance. Palaeogeography, Palaeoclimatology, Palaeoecology 146, 1–18.

Kershaw, S., Guo, L., Swift, A., Fan, J., 2002. ?Microbialites in the Permian–Triassic boundary interval in central China: structure, age and distribution. Facies 47, 83–90.

Kershaw, S., Li, Y., Crasquin-Soleau, S., Feng, Q.L., Mu, X.N., Collin, P.Y., Reynolds, A., Guo, L., 2007. Earliest Triassic microbialites in the South China block and other areas: Controls on their growth and distribution. Facies 53, 409−425.

Kershaw, S., Crasquin, S., Forel, M.B., Randon, S., Collin, P.Y., Kosun, E., Richoz, S., Baud, A., 2011. Earliest Triassic microbialites in Çürük Dag, southern Turkey: composition, sequence and controls on formation. Sedimentology 58, 739−755.

Kershaw, S., Crasquin, S., Li, Y., Collin, P.Y., Forel, M.B., Mu, X., Baud, A., Wang, Y., Xie, S., Maurer, F., Guo, L., 2012. Microbialites and global environmental

775 change across the Permian-Triassic boundary: a synthesis. Geobiology 10, 25−47.
776 Lehrmann, D.J., 1999. Early Triassic calcimicrobial mounds and biostromes of the
777 Nanpanjiang Basin, South China. Geology 27, 359–362.
778 Lehrmann, D.J., Bentz, J.M., Wood, T., Goers, A., Dhillon, R., Akin, S., Li, X.W.,
779 Payne, J.L., Kelley, B.M., Meyer, K.M., Schaal, E.K., Suarez, M.B., Yu, M.Y.,
780 Qin, Y.J., Li, R.X., Minzoni, M., Henderson, C.M., 2015. Environmental controls
781 on the genesis of marine microbialites and dissolution surface associated with the
782 end-Permian mass extinction: new sections and observations from the
783 Nanpanjiang Basin, South China. Palaios 30, 529−552.
784 Li, G., Wang, Y., Shi, G.R., Liao, W., Yu, L., 2016. Fluctuations of redox conditions
785 across the Permian-Triassic boundary: New evidence from the GSSP section in
786 Meishan of South China. Palaeogeography, Palaeoclimatology, Palaeoecology
787 448, 48−58.
788 Liao, W., Wang, Y.B., Kershaw, S., Wang, Z.T., Yang, H., 2010. Shallow-marine
789 dysoxia across the Permian−Triassic boundary: evidence from pyrite framboids in
790 the microbialite in South China. Sedimentary Geology 232, 77−83.
791 Lith, Y.V., Warthmann, R., Vasconcelos, C., Mackenzie, J.A., 2003. Microbial
792 fossilization in carbonate sediments: a result of the bacterial surface involvement
793 in dolomite precipitation. Sedimentology 50, 237−245.
794 Loope, G.R., Kump, L.R., Arthur, M.A., 2013. Shallow water redox conditions from
795 the Permian−Triassic boundary microbialite: the rare earth element and iodine
796 geochemistry of carbonates from Turkey and South China. Chemical Geology
797 351, 195−208.
798 Luo, M., Chen, Z.Q., Hu, S.X., Zhang, Q.Y., Benton, M.J., Zhou, C.Y., Wen, W.,
799 Huang, J.Y., 2013. Carbonate reticulated ridge structures from the lower Middle

800 Triassic of the Luoping area, Yunnan, southwestern China: geobiological features
801 and implications for exceptional preservation of the Luoping biota. Palaios 28,
802 541−551.
803 Luo, M., Chen, Z.Q., Zhao, L.S., Kershaw, S., Huang, J.Y., Wu, L.L., Yang, H., Fang,
804 Y.H., Huang, Y.G., Zhang, Q.Y., Hu, S.X., Zhou, C.Y., Wen, W., Jia, Z.H., 2014.
805 Early Middle Triassic stromatolites from the Luoping area, Yunnan Province,
806 Southwest China: geobiologic features and environmental implications.
807 Palaeogeography, Palaeoclimatology, Palaeoecology 412, 124−140.
808 Luo, M., Chen, Z.Q., Shi, G.R., Fang, Y.H., Song, H.J., Jia, Z.H., Huang, Y.G., Yang,
809 H., 2016a. Upper Lower Triassic stromatolite from Anhui, South China:
810 geobiologic features and paleoenvironmental implications. Palaeogeography,
811 Palaeoclimatology, Palaeoecology 452, 40−54.
812 Luo, M., George, A.D., Chen, Z.Q., 2016b. Sedimentology and ichnology of two
813 Lower Triassic sections in South China: Implications for the biotic recovery
814 following the end-Permian mass extinction. Global and Planetary Change 144,
815 198−212.
816 Ma, D.R., 2016. Uppermost Permian to Lower Triassic conodonts from the Tieshikou
817 section, southern Jiangxi Province and Selong section, southern Tibet, China.
818 Unpublished Master Thesis of China University of Geosciences, China
819 University of Geosciences (Wuhan), Wuhan, 166 pp.
820 Magaritz, M., Holser, W.T., 1991. The Permian−Triassic of the Gartnerkofel-1 Core
821 (Carnic Alps, Austria): Carbon and oxygen isotope variation. Abhandlungen der
822 Geologischen Bundesanstalt Wien 45, 149−163.
823 McCrea, J.M., 1950. The isotopic chemistry of carbonates and a paleotemperature
824 scale. The Journal of Chemical Physics 18, 849−857.

825 Monty, C.L.V., 1995. The rise and nature of carbonate mud-mound: an introductory
826 actualistic approach. In: Monty, C.L.V., Bosence, D.W.J., Swells, P.H.B., Pratt,
827 B.R. (Eds), Carbonate Mud-mound: Their Origin and Evolution. International
828 Association of Sedimentologist, Special Publication Volume 23, pp. 11−48.
829 Neu, T.R., Lawrence, J.R., 2015. Innovative techniques, sensors and approaches for
830 imaging biofilms at different scales. Trends in Microbiology 23, 233–242.
831 Neu, T.R., Manz, B., Volke, F., Dynes, J.J., Hitchcock, A.P., Lawrence, J.R., 2010.
832 Advanced imaging techniques for assessment of structure, composition and
833 function in biofilm systems. FEMS Microbiology Ecology 72, 1–21.
834 Noffke, N., 2010. Geobiology: Microbial Mats in Sandy Deposits from the Archean
835 Era to Today. Springer, 193 pp.
836 Noffke, N., Gerdes, G., Klenke, T., 2003. Benthic cyanobacteria and their influence on
837 the sedimentary dynamics of peritidal depositional systems (siliciclastic,
838 evaporitic salty and evaporitic carbonate). Earth-Science Reviews 12, 1−14.
839 Pei, Y., Chen, Z.Q., Fang, Y.H., Kershaw, S., Wu, S.Q., Luo, M., 2018. Volcanism,
840 redox conditions, and microbialite growth linked with the end-Permian mass
841 extinction: evidence from the Xiajiacao section (western Hubei Province), South
842 China. Palaeogeography, Palaeoclimatology, Palaeoecology (this volume, in
843 press), http://dx.doi.org/10.1016/j.palaeo.2018. 01.043.
844 Pruss, S.B., Bottjer, D.J., Corsetti, F.A., Baud, A., 2006. A global marine sedimentary
845 response to the end-Permian mass extinction: examples from southern Turkey and
846 the Western United States. Earth-Science Reviews 78, 193−206.
847 Reid, P., Visscher, P.T., Decho, A.W., Stolz, J.F., Bebout, B. M., Dupraz, C.,
848 Macintyre, I. G., Paerl, H.W., Pinckney, J.L., Prufert-Bebout, L., Steppe, T.F.,
849 DesMarais, D.J., 2000. The role of microbes in accretion, lamination and early

lithification of modern marine stromatolites. Nature 406, 989−992.

Riding, R., 2006. Microbial carbonate abundance compared with fluctuations in metazoan diversity over geological time. Sedimentary Geology 185, 229−238.

Riding, R., 2008. Abiogenic, microbial and hybrid authigenic carbonate crusts: components of Precambrian stromatolites. Geologia Croatica 61(2−3), 73−103.

Riding, R., 2011. The nature of stromatolites: 3,500 million years of history and a century of research. In: Reitner, J., Nadia-Valérie, Q., Arp, G. (Eds), Lecture Notes in Earth Sciences, Vol. 131, Springer, Berlin, pp. 29−74.

Riding, R., Liang, L., 2005. Geobiology of microbial carbonates: metazoan and seawater saturation state influences on secular trends during the Phanerozoic. Palaeogeography, Palaeoclimatology, Palaeoecology 219, 101−115.

Saito, R., Oba, M., Kaiho, K., Schaeffer, P., Adam, P., Takahashi, S., Nara, F.W., Chen, Z.Q., Tong, J.N., Tsuchiya, N., 2014. Predominance of archaea-derived hydrocarbons in an Early Triassic microbialite. Organic Geochemistry 73, 113−122.

Sanz-Montero, M.E., Rodriguez-Aranda, J.P., Perez-Soba, C., 2008. Microbial weathering of Fe-rich phyllosilicates and formation of pyrite in the dolomite precipitating environment of a Miocene lacustrine system. European Journal of Mineralogy 21, 163−175

Sheng, J., Chen, C., Wang, Y., Rui, L., Liao, Z., Bando, Y., Ishii, K., Nakazawa, K., Nakamura, K., 1984. Permian−Triassic boundary in Middle and Eastern Tethys. Journal of the Faculty of Science, Hokkaido University, Series 4: Geology and Mineralogy 21, 133−181.

Shiraishi, F., Bissett, A., Beer, D. de, Reimer, A., Arp, G., 2008. Photosynthesis, respiration and exopolymer calcium-binding in biofilm calcification (Westerhöfer

and Deinschwanger Creek, Germany). Geomicrobiology Journal 25(2), 83–94.

Sun, C.L., 1988. Early Triassic stratigraphy in Jiangxi Province, Journal of Stratigraphy 12, 39−47.

Sun, S., Li, J.L., Chen, H.H., Peng, H.P., Hsu, K.J., Shelton, J.W., 1989. Mesozoic and Cenozoic sedimentary history of South China. American Association of Petroleum Geologists, Bulletin 73, 1247−1269.

Seong-Joo, L., Browne, K.M., Golubic, S., 2000. On stromatolite lamination. In: Riding, R., Awramik, S.M. (Eds), Microbial Sediments. Springer-Verlag, Berlin-Heidelberg, pp. 16−24.

Tang, H., Kershaw, S., Liu, H., Tan, X.C., Li, F., Hu, G., Huang, C., Wang, L.C., Lian, C.B., Li, L., Yang, X.F., 2017. Permian–Triassic boundary microbialites (PTB-microbialites) in southwest China: implications for paleoenvironment reconstruction. Facies 63, 2e.

Tu, C.Y., Chen, Z.Q., Retallack, G.J., Huang, Y.G., Fang, Y.H., 2016. Proliferation of MISS related microbial mats following the end-Permian mass extinction in terrestrial ecosystems: Evidence from the Lower Triassic of the Yiyang area, Henan Province, North China. Sedimentary Geology 333, 50−69.

Visscher, P.T., Reid, R.P., Bebout, B.M., 2000. Microscale observation of sulphate reduction: correlation of microbial activity with lithified micritic laminae in modern marine stromatolites. Geology 28, 919−922

Wang, Y.B., Tong, J., Wang, J.S., Zhou, X.G., 2005. Calcimicrobialite after end-Permian mass extinction in South China and its palaeoenvironmental significance. Chinese Science Bulletin 50, 665−671.

Woods, A.D., 2014. Assessing Early Triassic paleoceanographic conditions via unusual sedimentary fabrics and features. Earth-Science Reviews 137, 6−18

900 Woods, A.D., Baud, A., 2008. Anachronistic facies from a drowned Lower Triassic
901 carbonate platform: lower member of the Alwa Formation (Báid Exotic), Oman
902 Mountains. Sedimentary Geology 209, 1−14.
903 Woods, A.D., Bottjer, D.J., Mutti, M., Morrison, J., 1999. Lower Triassic large
904 sea-floor carbonate cements: their origin and a mechanism for the prolonged
905 biotic recovery from the end-Permian mass extinction. Geology 27, 645−648.
906 Woods, A.D., Bottjer, D.J., Corsetti, F.A., 2007. Calcium carbonate seafloor
907 precipitates from the outer shelf to slope facies of the Lower Triassic
908 (Smithian-Spathian) Union Wash Formation, California, U.S.A.: sedimentology
909 and palaeobiologic significance. Palaeogeography, Palaeoclimatology,
910 Palaeoecology 252, 281−290.
911 Wu, G.C., Yao, J.X., Ji, Z.S., 2003. Conodont fauna of late Upper Permian in Xinfeng
912 area, Jiangxi Province. Acta Scientiarum Naturalium Universitatis Pekinensis 39,
913 211−218.
914 Wu, S.Q., Chen, Z.Q., Fang, Y.H., Pei, Y., Yang, H., Ogg, J., 2017. A
915 Permian−Triassic boundary microbialite deposit from the eastern Yangtze Platform
916 (Jiangxi Province, South China): Geobiologic features, ecosystem composition and
917 redox conditions. Palaeogeography, Palaeoclimatology, Palaeoecology 486, 58−73.
918 Wu, Y.S., 1991. Calcareous algae from Permian reefs of Longlin, Guangxi, China.
919 Acta Palaeontologica Sinica 30, 750−771.
920 Wu, Y.S., Yu, G.L., Li, R.H., Song, L.R., Jiang, H.X., Riding, R., Liu, L.J., Liu, D.Y.,
921 Zhao, R., 2014. Cyanobacterial fossils from 252 Ma old microbialites and their
922 environmental significance. Scientific Reports 4, 3820e.
923 Wu, Y.S., Yu, G.L., Jiang, H.X., Liu, L.J., Zhao, R., 2016. Role and lifestyle of
924 calcified cyanobacteria (*Stanieria*) in Permian-Triassic boundary microbialites.

925 Palaeogeography, Palaeoclimatology, Palaeoecology 448, 39−47.
926 Xie, S.C., Pancost, R.D., Yin, H.F, Wang, H.M., Evershed, R.P., 2005. Two episodes
927 of microbial change coupled with Permo/Triassic faunal mass extinction. Nature
928 434, 494−497.
929 Xu, Y.L., Chen, Z.Q., Feng, X.Q., Wu, S.Q., Shi, G.R., Tu, C.Y., 2017. Proliferation
930 of MISS-related microbial mats following the end-Permian mass extinction in the
931 northern Paleo-Tethys: evidence from southern Qilianshan region, western China.
932 Palaeogeography, Palaeoclimatology, Palaeoecology 474, 198−213.
933 Yang, H., Chen, Z.Q., Wang, Y., Tong, J., Song, H., Chen, J., 2011. Composition and
934 structure of microbialite ecosystems following the end-Permian mass extinction
935 in South China. Palaeogeography, Palaeoclimatology, Palaeoecology 308,
936 111−128.
937 Yang, H., Chen, Z.Q., Ou, W.Q., 2015a. Microconchids from microbialites near the
938 Permian−Triassic boundary in the Zuodeng section, Baise area, Guangxi Province,
939 South China and their palaeoenvironmental implications. Journal of Earth
940 Science 26, 157−1965.
941 Yang, H., Chen, Z.Q., Wang, Y.B., Ou, W.Q., Liao, W., Mei, X., 2015b. Palaeoecology
942 of microconchids from microbialites near the Permian−Triassic boundary in
943 South China. Lethaia 48, 497−508.
944 Yin, H.F., Zhang, K., Tong, J., Yang, Z., Wu. S., 2001. The Global Stratotype Section
945 and Point (GSSP) of the Permian−Triassic boundary. Episodes 24, 102−114.
946 Zhao, L., Chen, Z.Q., Algeo, T.J., Chen, J., Chen, Y., Tong, J., Gao, S., Zhou, L., Hu,
947 Z., Liu, Y., 2013. Rare-earth element patterns in conodont albid crowns: evidence
948 for massive inputs of volcanic ash during the latest Permian biocrisis? Global and
949 Planetary Change 105, 135−151.

Zhu, X.S., Wang, C.Y., Lü, H., Mu, X.N., Zhang, L.X., Qin, Z.S., Luo, H., Yang, W., R., Deng, Z.Q., 1994. Permian−Triassic boundaries in Jiangxi, China. Acta Micropalaeontologica Sinica 11, 439−452.

Zhu, X.S., Zhang, D.F., Zhong, Y.X., 1999. Discoveries of the *Clarkina* from the P/T boundary clay bed in Taojiang section in southern Jiangxi. Journal of Jiangxi Normal University (Natural Science Edition) 23, 162−169.

Ziegler, A.M., Gibbs, M.T., Hulver, M.Z., 1998. A mini-atlas of oceanic water masses in the Permian Period. Proceedings of the Royal Society of Victoria 110, 323−343.

Figure and table captions

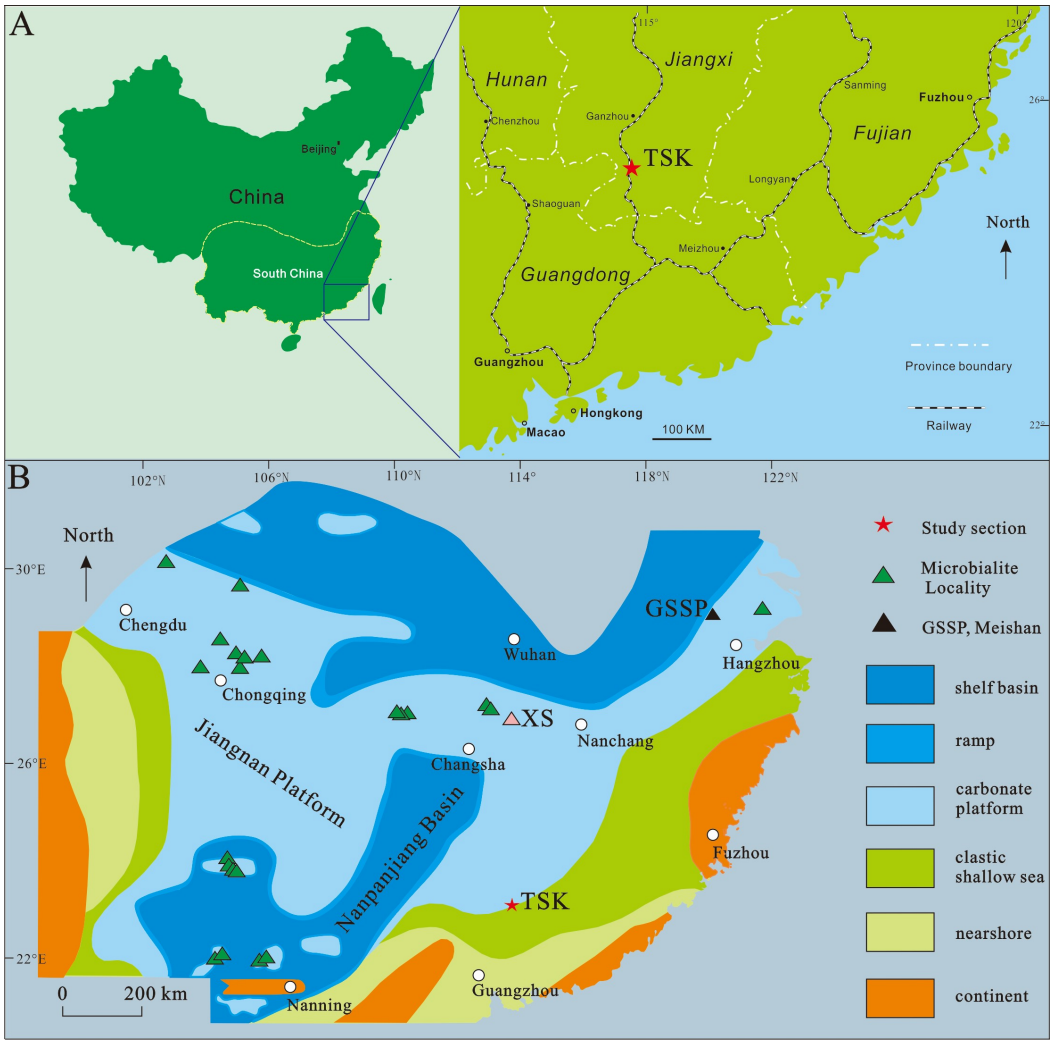

962

963 **Fig. 1.** (A) Location of the Tieshikou section in Xinfeng County, southern Jiangxi
964 Province, South China. (B) Paleogeographic configuration of the South China Block
965 during the P–Tr transition (Modified from Feng et al., 1997) showing location of the
966 study section and 38 other PTB microbialite sites across South China (Wu et al.,
967 2017). TSK: Tieshikou section; XS: Xiushui section; GSSP Meishan: Global
968 Stratotype of Section and Point of the Meishan section.

969

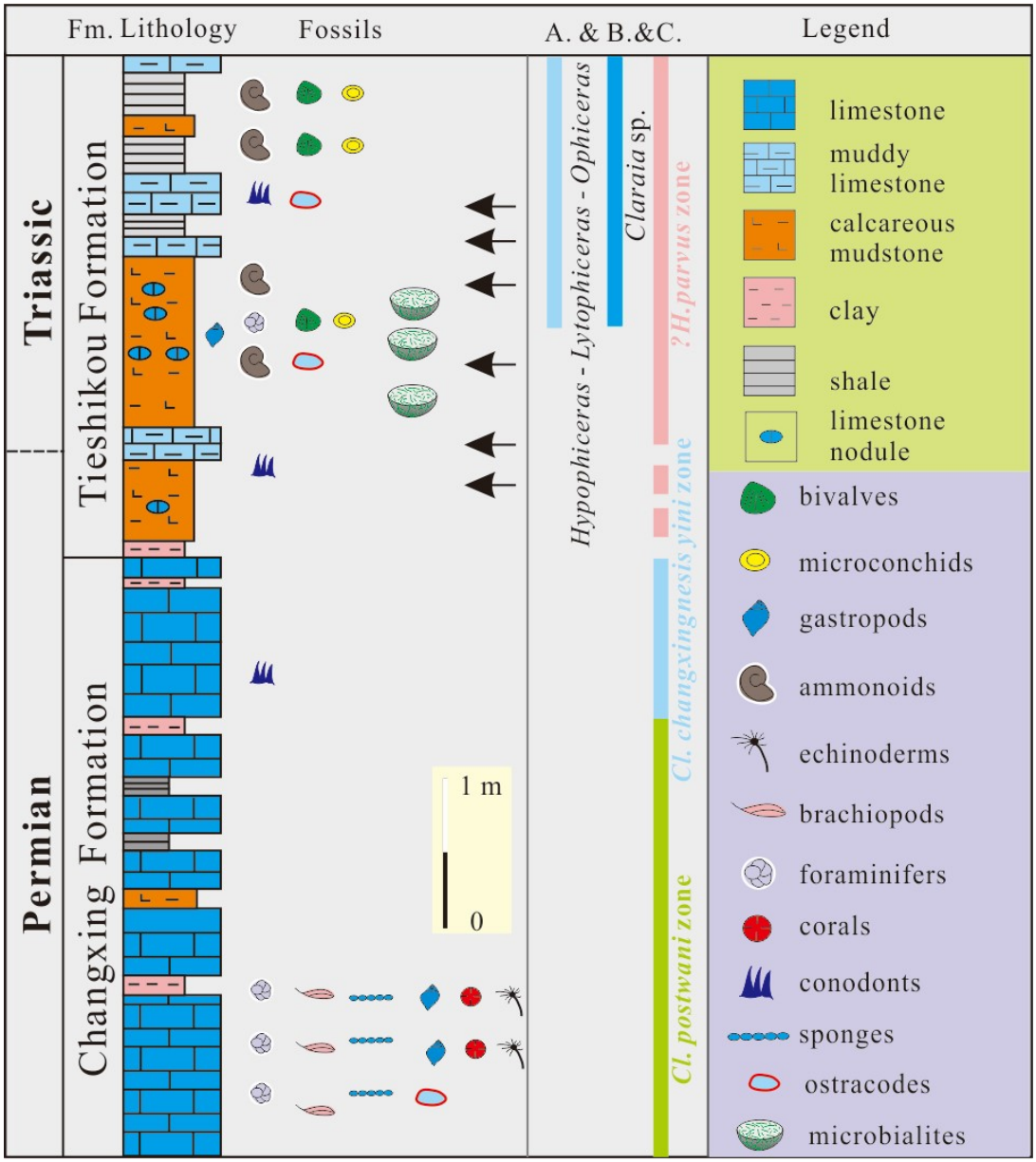

970

971 **Fig. 2.** The Permian−Triassic succession exposed at the Tieshikou section, showing
972 the stratigraphic distribution of various fossils, biozones, as well as the microbialite
973 horizon. Black arrows indicate sampling horizons for pyrite framboid analysis.
974 Conodont zones follow Zhu et al. (1999) and Wu et al. (2003), and bivalve and
975 ammonoid assemblages follow Sun (1988) and Zhu et al. (1994). A. = ammonoids, B.
976 = bivalves, C. = conodonts, Fm = Formation.

977

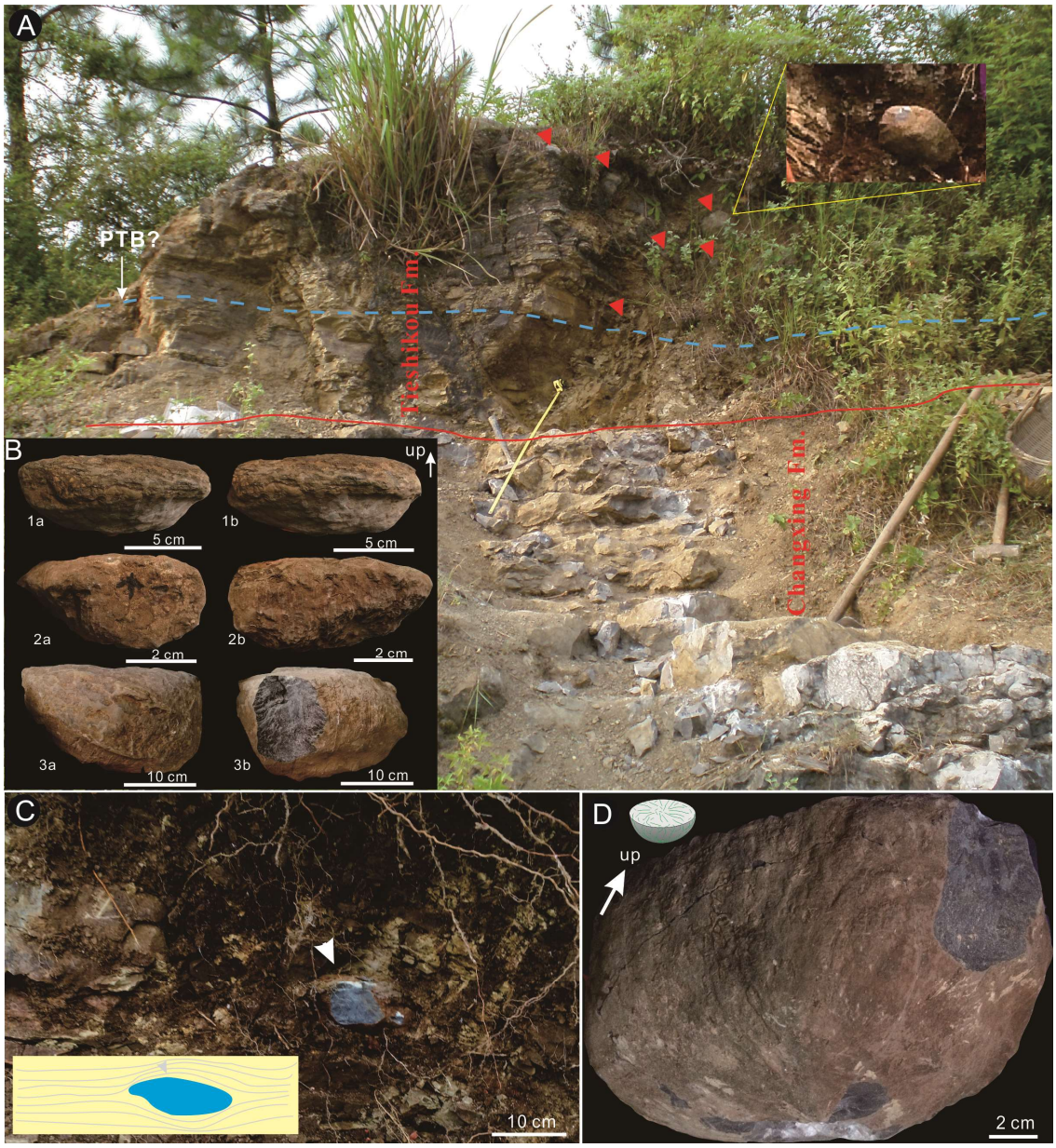

978

979 **Fig. 3. (**A) Field photo showing the Permian−Triassic boundary (PTB) succession at
980 the Tieshikou section. Note the blue line indicates the probable location of the PTB,
981 and the inserted photo at upper right corner shows a small microbialite embedded in a
982 mudstone layer (red arrows), 0.7 m above the PTB. (B) Three isolated bowl-like
983 nodules (B_1−B_3). Note that photos labeled a and b represent anterior and posterior
984 views, respectively. (C) Close-up of another small microbialite (white arrow)
985 embedded in a mudstone bed, 1.1 m above the PTB. Cartoon diagram in lower left
986 corner shows that horizontal laminae are deflected around the small microbialite. (D)

Close-up of the small microbialite in A, showing the bowl-like morphology (sees also cartoon diagram at upper left corner). Note that the arrow indicates upward direction.

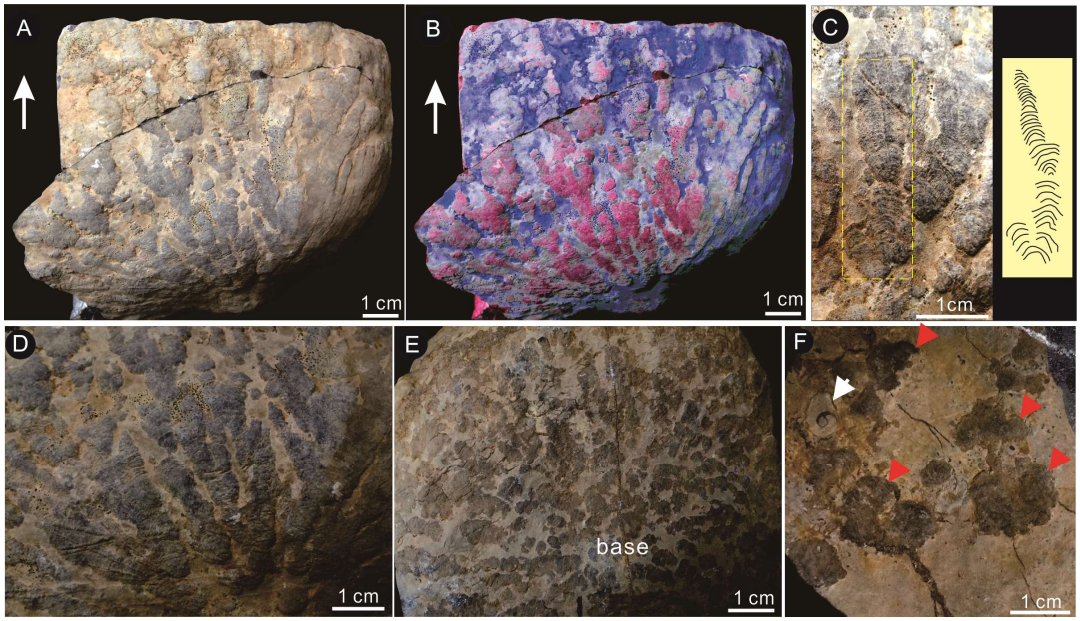

Fig. 4. Columnar stromatolites make up the bowl-like microbialites. **(**A) Side view of a small microbialite, showing dark colored columnar structures that frequently branch upward, demonstrating life position. (B) A false-color image of A (after Photoshop color enhancement) showing pronounced laminated and branching microbialite columns. (C) Close-up of a microbialite column, showing that the column is densely laminated and branches once. (D) Close-up of microbialite columns, showing that columns are densely laminated and branch frequently. (E) Base view of a bowl-like microbialite, showing microbial clots surrounding the core. (F) Close-up of the top of the bowl-like microbialite, showing cloud-like masses (red arrows) and an ammonoid shell (white arrow).

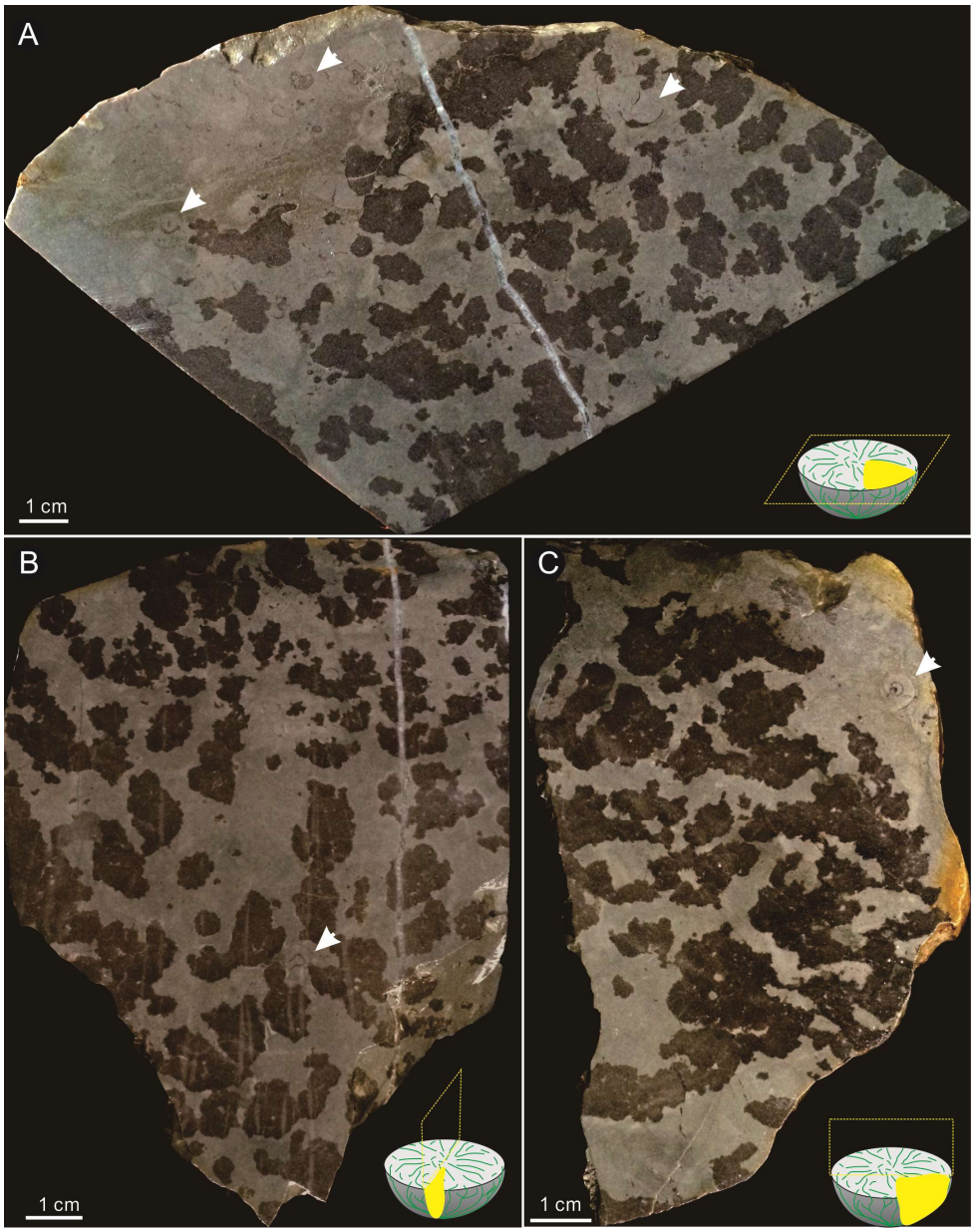

Fig. 5. Polished slabs of one bowl-like structure viewed from various angles. Note that cartoon diagrams in the lower right corner of the photographs show the sectioning directions of the slab. Ammonoid shells (white arrows) occur along the margins of the bowl-like structure or within the clotted texture. (A) Slab view of the microbialite cut parallel to bedding, showing microbial clots (dark colored areas) and surrounding micrite (gray areas). (B−C) Slab views of the microbialite cut perpendicular to bedding , showing clotted texture characterized by microbial clots (dark colored areas) and micrite (gray areas).

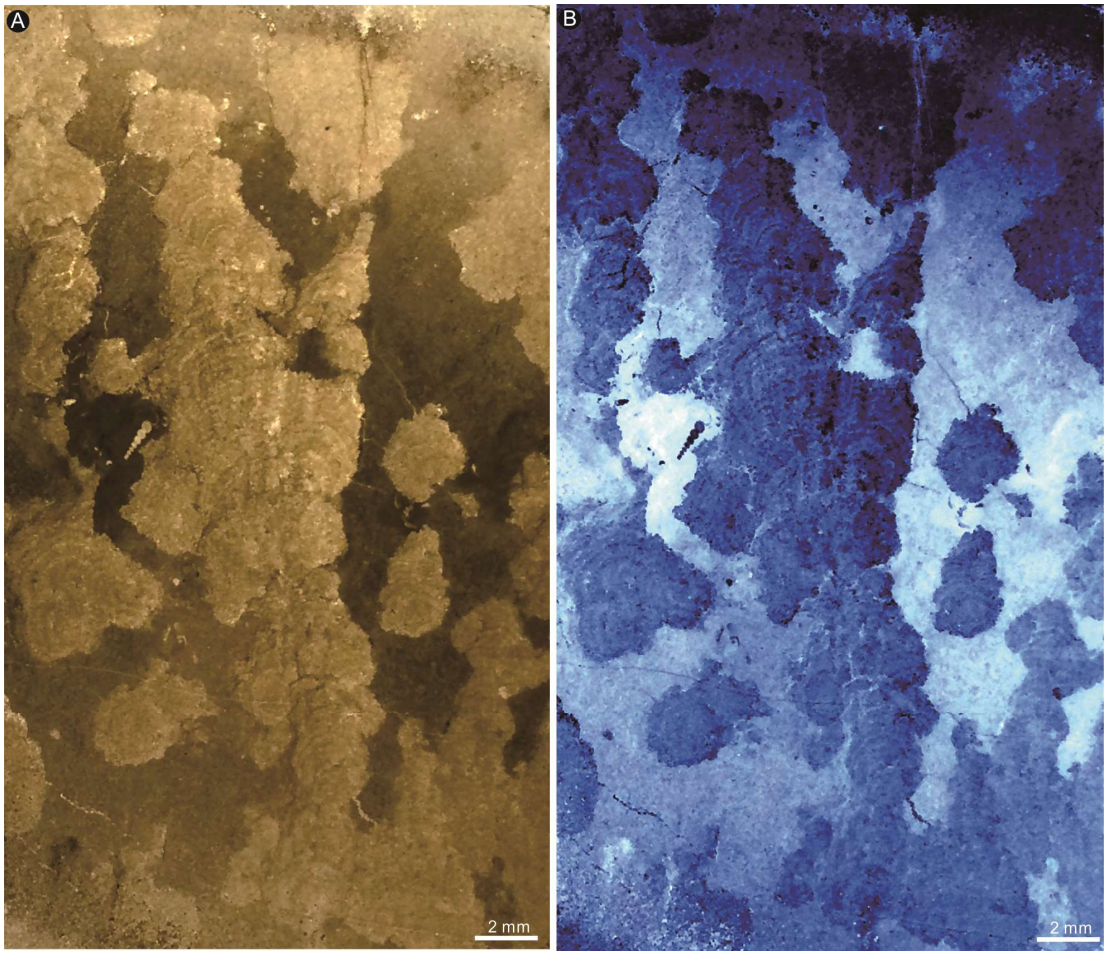

Fig. 6. Photomicrographs of bowl-like microbialite under plane polarized light (A) and a false-color image (after Photoshop color enhancement) (B) showing the densely laminated and frequently branching microbial columns (light colored in A and dark blue in B) and surrounding micrites (dark colored in A, and bright to light blue in B). Note that the false color helps to bring out some of the details of the thin section.

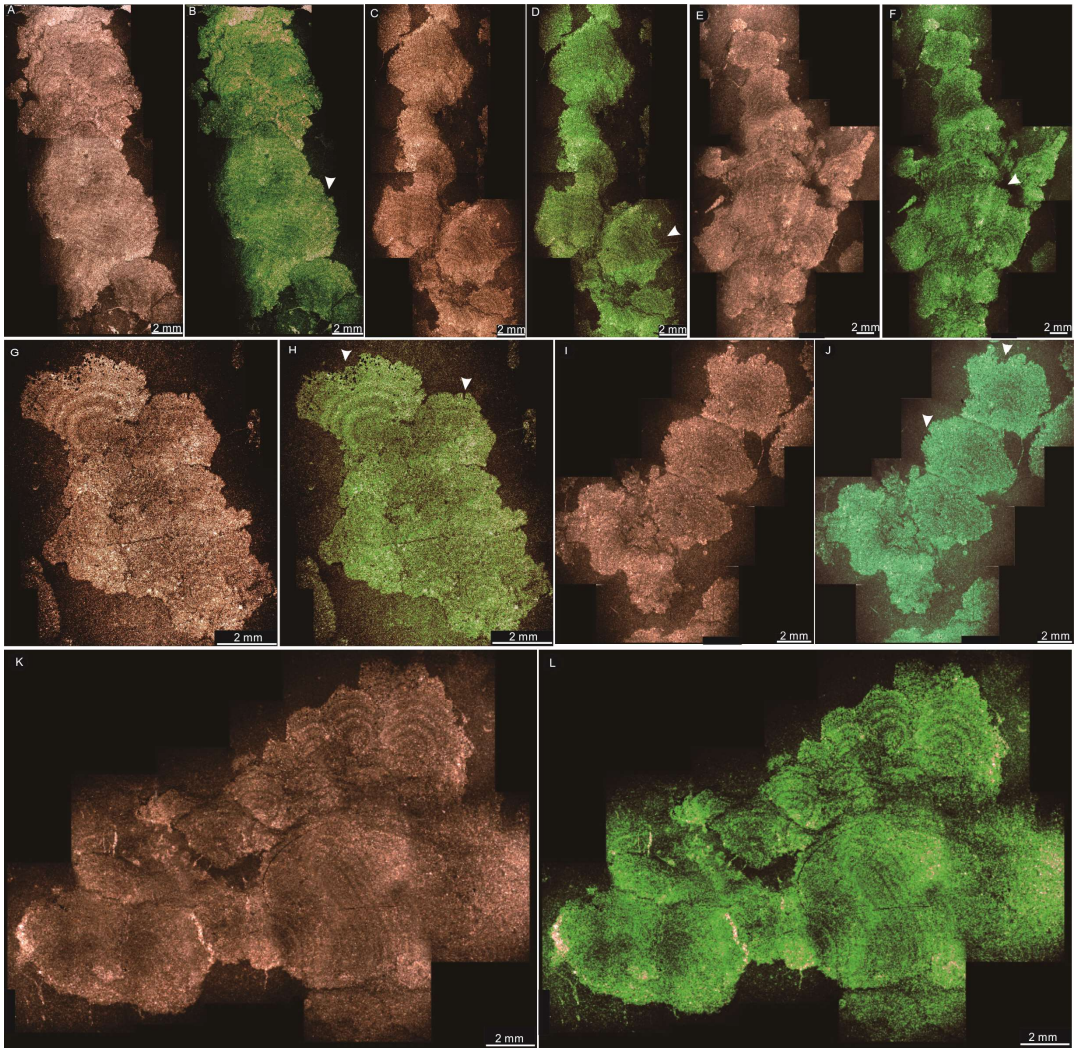

Fig. 7. Photomicrographs of the columnar stromatolites, showing various morphologies of the columns. Note that the brown-colored columns are photographed under plane polarized light, while the green-colored columns are Photoshop-enhanced. White triangles in B, D, F, H, and J indicate dissolution along the margins of fan structures or columns. (A−B) Single cylindrical in the lower part are massive to clotted, while three small columns cluster in the upper part cluster of the larger, cylindrical columns. (C−D) Two overlapping columns. (E−F) Dendritic columns that branch and generate smaller columns. (G−H) Microbialite columns with a mammillary texture; they are comprised of multiple crystal fans that have a radiating texture and show distinct growth laminae. Note that the radiating fans occur throughout these structures. (I−J) Three cement fans that stack on top of each other.

(K−L) Cabbage-shaped structures that cluster together, with distinct concentric laminar laminae within each fan.

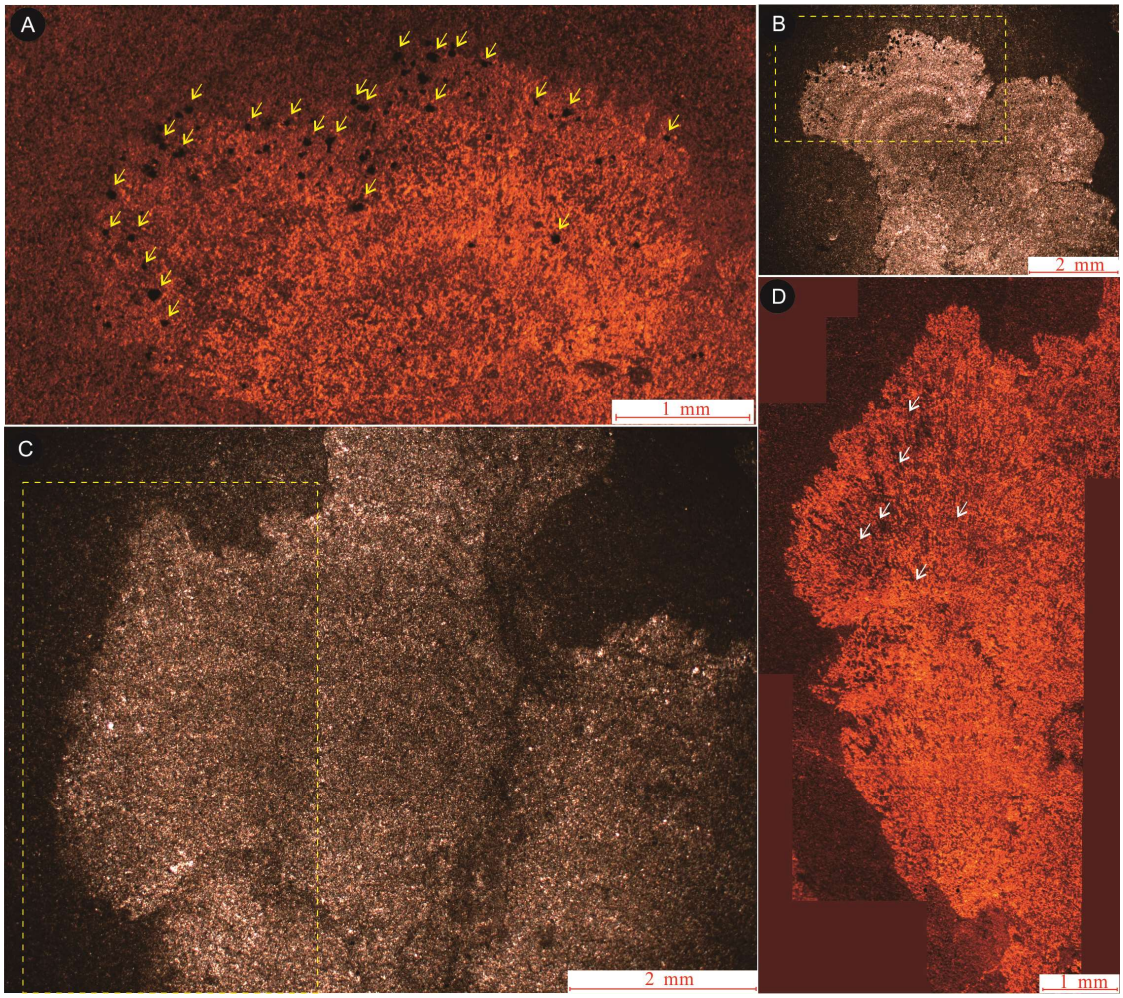

Fig. 8. Photomicrographs of microbialites in transmitted light and Cathodoluminescence (CL). (A) CL image showing close-up of the boxed area in B, illustrating concentric laminar and radiating structures within the cement fan, as well as pyrite grains (yellow arrows) that occur scattered in laminae or along margins of the cement fans. (B−C) Two fans at different orientations to each other, showing distinct concentric laminar structures and radiating lines. Note that dashed yellow squares in C show the areas illustrated in A and D, respectively. (D) CL image showing close-up of the boxed area in C, showing radiating rod-shaped structures on

1045 the cement fan.

1046

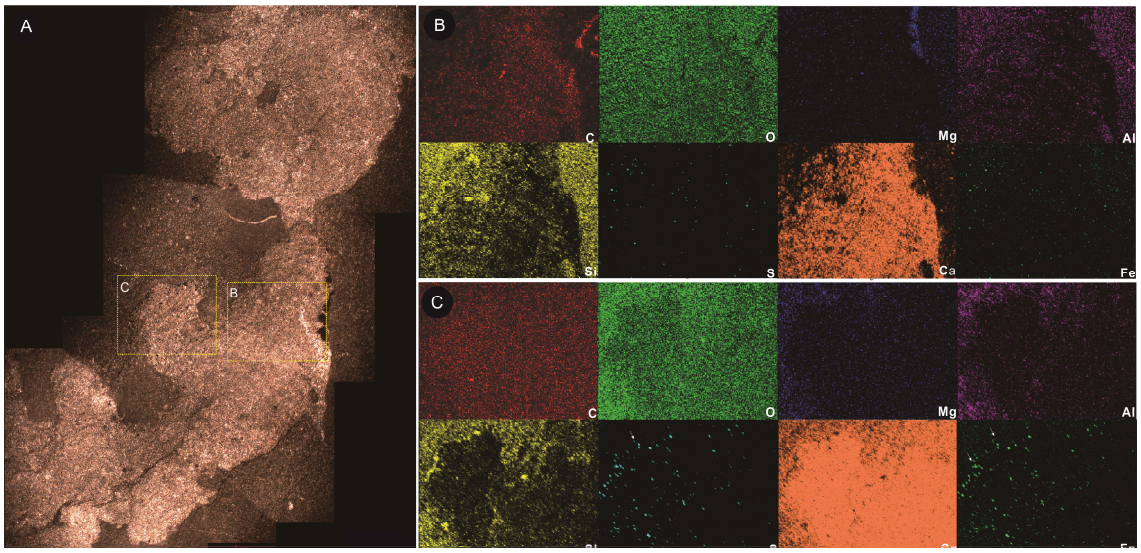

1047

1048 **Fig. 9.** Photomicrograph and EDS element mapping images of cement fan structures.
1049 (A) Photomicrograph of microbialite columns. Note the yellow squares B and C show
1050 the EDS element mapping areas. (B) EDS element map images of the boxed area (B)
1051 in A, showing the concentrations of C, O, Mg, Al, Si, S, Ca, and Fe. (C) EDS element
1052 map images of the boxed area (C) in A, showing concentrations of C, O, Mg, Al, Si, S,
1053 Ca, and Fe. Note that thin sections were etched with acetic acid.

1054

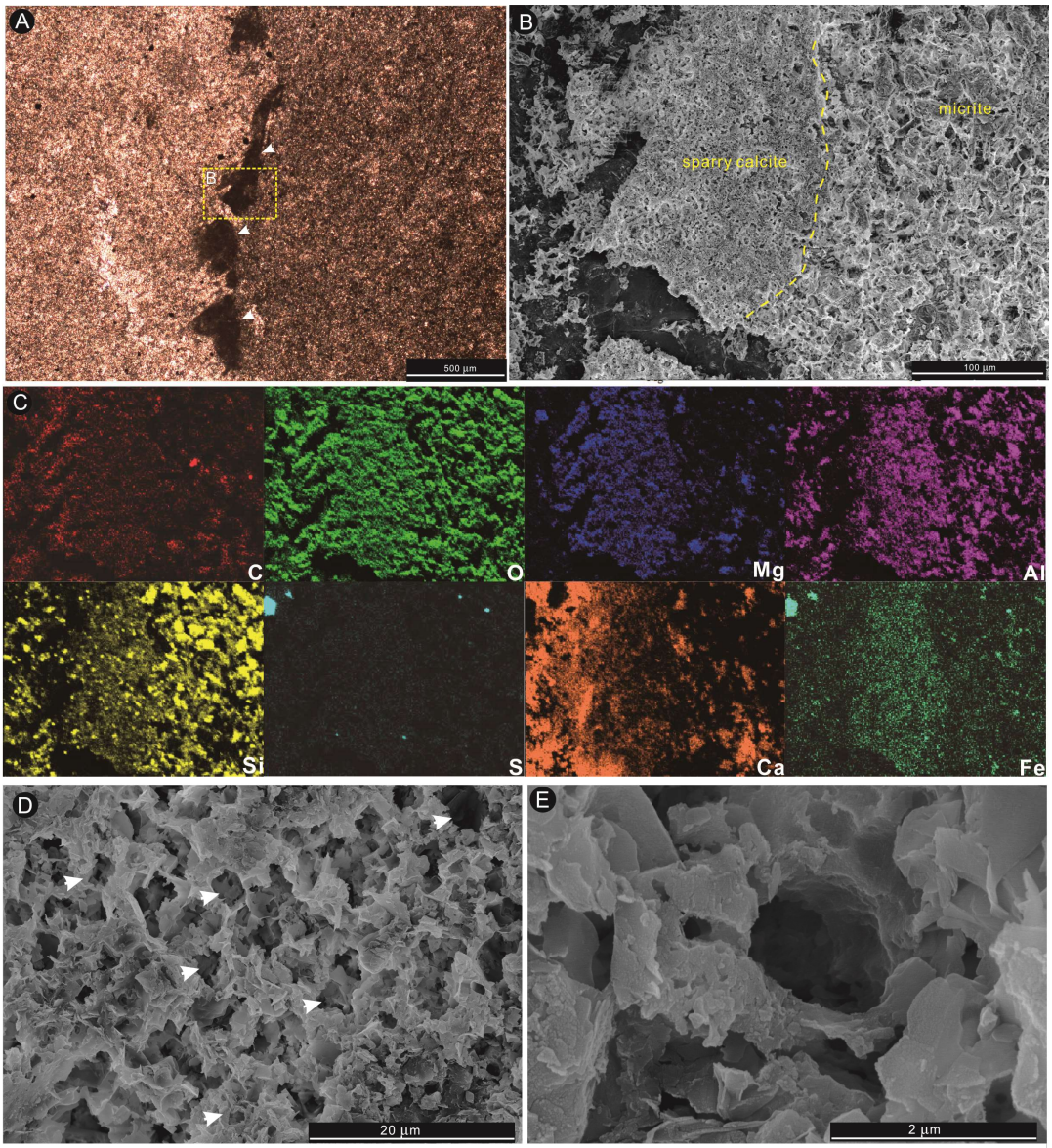

Fig. 10. Photomicrograph and SEM images of the junction between sparry calcites and micrites within a microbial column. (A) Photomicrograph showing the contact (white arrows) between sparry cement calcites and micrites. (B) SEM image of boxed area in A, showing the boundary (dashed yellow lines) between micrite and sparry calcite. (C) EDS element maps of C, O, Mg, Al, Si, S, Ca, Fe, and it shows contents of Ca, Mg, O, Al, and Si within sparry calcite cement. (D) SEM image showing nano-sized particles, representing calcified extracellular polymeric substances (EPS), and they interweave to form pore structures that are surrounded by walls made up of a mixture of calcium carbonate and silicates. White arrows indicate micro-pore

1065 structures. (E) Close-up of a pore structure.

1066 .

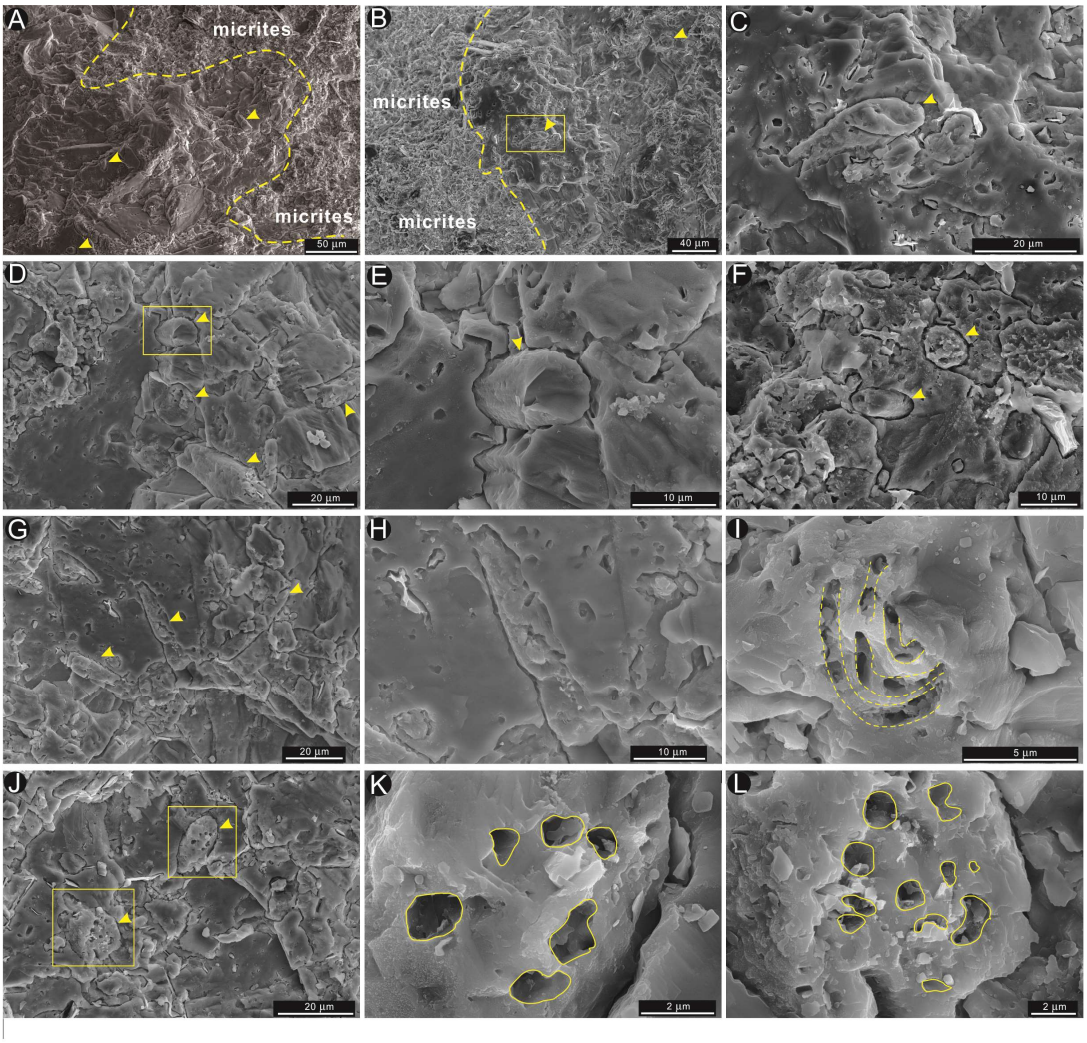

1067

1068 **Fig. 11.** SEM images of rod-shaped objects and filament sheaths preserved in the
1069 microbialite. (A−B) Close-up of clotted textures in microbialite, showing the contact
1070 between micrite and sparite (dashed yellow line) and rod-shaped objects (yellow
1071 arrows) on sparry calcite. (C) Close-up of boxed area in B showing a rod-shaped
1072 object that has a smooth surface and a depression in cross section. (D) Another
1073 rod-shaped object within sparry calcite. E) Close-up of boxed area in D, showing a
1074 rod-shaped object that has a smooth surface and a depression in cross section. F) Two
1075 rod-shaped objects in vertical profile view. Note that the object on the left has a
1076 smooth surface and depressed end, while the object on the right has multiple

micropores in cross section. (G) Three rod-shaped objects in horizontal plane view. (H) Close-up of the middle rod in G showing irregular corrosion traces on its surfaces. (I) Worm-like filament sheaths on sparry calcite. (J) Two rods in vertical profile view showing multiple micropores in cross section of the rod. (K−L) Close-ups of boxed areas in J, showing prominent micropores, 0.5−1.0 μm in diameter, in cross section of a rod.

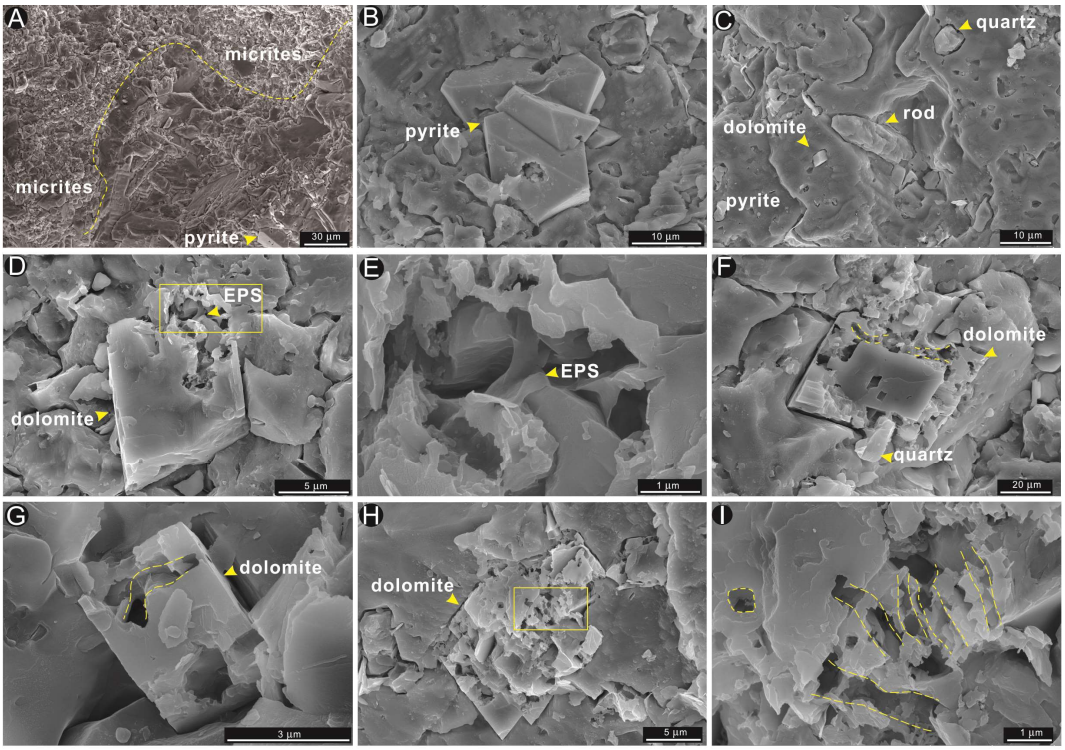

Fig. 12. SEM images nano-sized particles on surfaces of pyrite crystals and dolomite crystals embedded in microbialite. (A) SEM image showing the contact between micrites and sparry calcite. Note that some pyrite crystals occur in the sparry calcites. (B) Pyrite crystals with corroded surfaces. (C) Dolomite, quartz, and rod-shaped objects on sparry calcites within the microbialite. (D) Dolomite crystal with a broken corner from which abundant biofilms, probably representing extracellular polymeric substances (EPS), are exposed. (E) Close-up of boxed area in D, showing details of

EPS. (F) One dolomite crystal with a dense, dark colored core and corroded margins, with linear filament sheaths (outlined by dash lines). Note one small quartz grain (arrow) inserted in the margin of dolomite crystal. (G) Filament sheaths (yellow dashed lines) cross the surface of the dolomite crystal and penetrate into the dolomite. (H) Strongly corroded dolomite crystal with filament sheaths running through the grain. (I) Close-up of boxed area in H, showing nano-sized, linear filament sheaths on the surface and running through the crystal.

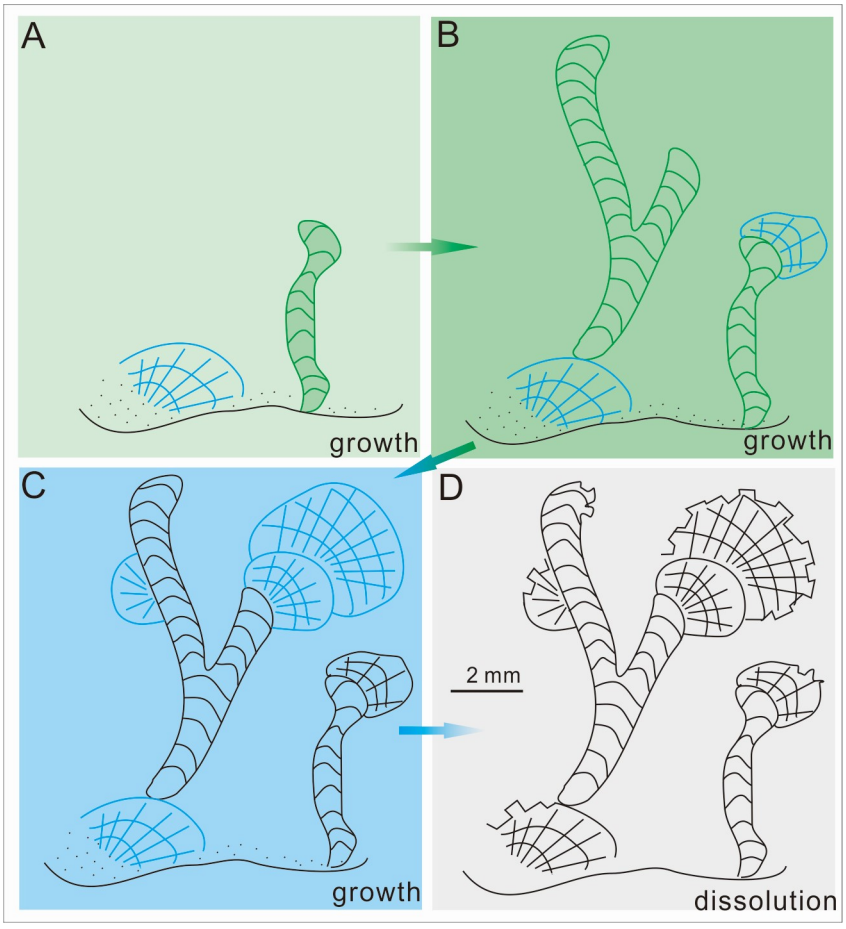

Fig. 13. Cartoon diagram showing the growth and dissolution of laminated columns and cement fans. (A) An isolated cement fan and laminated column grow on a siliciclastic sea-floor. (B) A new laminated column grows on the edge of a cement fan (left) and branches. Meanwhile, the laminated column gives rise to a new cement fan

(right). (C) The laminated column on the left also gives rise to a cement fan that continues to grow and forms a second generation cement fan, while the right laminated column structure ceases its growth. (D) Corrosion of edges of laminated columns and cement fans due to a submarine dissolution event.

Table 1. Carbon and oxygen isotopic compositions of laminated columns, cement fans, and micrites.

	$\delta^{13}C$ (‰)	$\delta^{18}O$ (‰)
Laminae microbialites	+0.05	–8.11
	–0.23	–7.92
	–0.54	–8.16
	–0.17	–7.68
Fans	–0.82	–8.19
	+0.02	–8.23
micrites	–0.96	–7.99
	–0.91	–8.47
	–0.92	–8.05